Received: 15 May 2022 | Revised: 20 October 2022 | Accepted: 21 October 2022

DOI: 10.1002/stc.3143

RESEARCH ARTICLE

WILEY

Robust optimal sensor configuration using the value of information

Sergio Cantero-Chinchilla[1] | **Costas Papadimitriou**[2] | **Juan Chiachío**[3] | **Manuel Chiachío**[3] | **Petros Koumoutsakos**[4,5] | **Adriano T. Fabro**[6] | **Dimitrios Chronopoulos**[7]

[1]Department of Mechanical Engineering, University of Bristol, Bristol, BS8 1TR, UK

[2]Department of Mechanical Engineering, University of Thessaly, Volos, Greece

[3]Department of Structural Mechanics & Hydraulics Engineering, Andalusian Research Institute in Data Science and Computational Intelligence (DaSCI), University of Granada, Granada, 18001, Spain

[4]School of Engineering and Applied Sciences, Harvard University, 29 Oxford Street, Cambridge, 02138, Massachusetts, USA

[5]Computational Science and Engineering Laboratory, ETH Zürich, Clausiusstrasse 33, Zürich, CH-8092, Switzerland

[6]Department of Mechanical Engineering, University of Brasilia, Brasilia, Brazil

[7]Department of Mechanical Engineering & Mecha(tro)nic System Dynamics (LMSD), KU Leuven, Gent, 9000, Belgium

Correspondence
Sergio Cantero-Chinchilla, Department of Mechanical Engineering, University of Bristol, Bristol BS8 1TR, UK.
Email: sergio.canterochinchilla@bristol.ac.uk

Funding information
European Union's Horizon 2020 Research and Innovation Programme under the Marie Skłodowska-Curie, Grant/Award Number: 721455; Brazilian National Council of Research CNPq, Grant/Award Number: 314168/2020-6

Abstract

Sensing is the cornerstone of any functional structural health monitoring technology, with sensor number and placement being a key aspect for reliable monitoring. We introduce for the first time a robust methodology for optimal sensor configuration based on the value of information that accounts for (1) uncertainties from updatable and nonupdatable parameters, (2) variability of the objective function with respect to nonupdatable parameters, and (3) the spatial correlation between sensors. The optimal sensor configuration is obtained by maximizing the expected value of information, which leads to a cost-benefit analysis that entails model parameter uncertainties. The proposed methodology is demonstrated on an application of structural health monitoring in plate-like structures using ultrasonic guided waves. We show that accounting for uncertainties is critical for an accurate diagnosis of damage. Furthermore, we provide critical assessment of the role of both the effect of modeling and measurement uncertainties and the optimization algorithm on the resulting sensor placement. The results on the health monitoring of an aluminum plate indicate the effectiveness and efficiency of the proposed methodology in discovering optimal sensor configurations.

KEYWORDS

guided waves, optimal sensor configuration, prediction model error, robust optimization, structural health monitoring, value of information

1 | INTRODUCTION

Structural health monitoring (SHM) refers to the development of *online* and *automated* damage detection, localization, and identification capability for aerospace, civil, and mechanical infrastructures. Sensing is the cornerstone of any functional SHM technology, with sensor number and positioning being a decision of great importance not only for reliable monitoring but also for cost efficiency. Indeed, despite the additional redundancy of acquired information, which is desirable to a certain degree, employing more sensors than the required minimum increases the monitoring cost, weight, volume, and complexity implied by the SHM system.[1] Thus, the minimum number of sensors along with their optimal positioning on the structural ensemble need to be decided during the design stage of an efficient SHM system. However, this decision cannot be reached without accounting for operational, environmental, and manufacturing-induced variability of the inspected system. The accuracy of the health monitoring is influenced by uncertainty associated with measurement errors and the relative size of damage in relation to the accuracy of the sensing system.[2,3] Therefore, a comprehensive methodology accounting for these uncertainties is required if a robust optimization of the number and positioning of sensors is desired.[1]

In the literature, a number of SHM approaches have been proposed in the last three decades,[4] including automated visual inspection techniques,[5] vibration response methods,[6] acoustic response approaches,[7] local stress, strain and admittance measurement approaches,[8] ultrasonic testing,[9,10] and temperature and chemical response methods.[11] Among them, ultrasonic guided waves have emerged as one of the most prominent candidates for continuous inspection of large plate-like structures and have attracted substantial industrial and academic attention.[12,13] The advantages of guided wave-based techniques include the employment of relatively cheap and light transducers able to interrogate large structural areas with a limited number of actuators and sensors. These active sensing techniques typically have a controllable frequency bandwidth whose signal features lie outside those from the environmental and operational regimes. This implies that no data normalization is required for the obtained measurements and no false alarms may arise due to external vibrations. Moreover, the excitation frequency can be tuned to be high enough to ensure interaction with small damage sizes[14] and low enough to avoid interference with stopbands[15] and inhomogeneities. Temperature variations with respect to baseline measurements can also be compensated by signal stretching.[16] Notwithstanding, the drawbacks of guided-wave deployment are mainly related to added complexity and weight implied by the utilization of cables, electronic management units, and power sources, as well as to the postprocessing complexity that is exacerbated when higher order modes are excited.[17] Minimizing these drawbacks can be tackled through a precise understanding of the wave characteristics and judicious selection and placement of transducers.

The optimization of sensor layouts for ultrasonic guided wave-based SHM systems has been addressed, for both active and passive sensing diagnosis, by maximizing specific performance indexes.[18–20] One relevant example is the *area of coverage* index, which typically relies on geometrical and physical properties of the plate and the guided waves.[21–23] This index has proven its effectiveness by combining numerical, experimental, and analytical information[24] for the optimization procedure. The typical optimization procedure used in these works relies on combinatorial algorithms such as genetic algorithms,[19,25] simulated annealing,[18,26] or particle swarm optimization,[27] which provide a *suboptimal* sensor layout with no indication of its accuracy. The *probability of detection* is another performance index which typically uses *ad hoc* features within the optimization methodology such as the distance of the damage from the sensor[28] or the strain caused by an impact.[29] More recently, a methodology to optimize the sensor location for both predictable and unpredictable damage locations has been provided based on the minimization of the scattered wave attenuation.[30] Nonetheless, none of these approaches have considered the uncertainty present in the data and also in the guided wave-related model, thus limiting its robustness against noise or parameter uncertainty.

Alternatively, Bayesian approaches have been proven to address the optimal sensor placement problem by quantifying uncertainty using the Kullback–Leibler (KL) divergence between the prior and posterior distribution as a measure of the information gain,[31,32] the Shannon information entropy of the posterior distribution as an estimate of the uncertainty of posterior information,[33–35] and the mutual information[36,37] between data and model parameters. It is important to remark that the aforementioned information theoretic approaches imply the definition of complex numerical optimization problems.[37] More recently, an efficient optimization of sensors and actuators in number and position has been proposed by using a convex entropy-based objective function.[38] Moreover, the *value of information*[39,40] has been adopted to optimize spatially distributed sensor systems, since it allows us accounting for information propagation among sensors (i.e., one location provides information used to update the other locations),[41] although with known submodularity issues, which make that the benefit of adding new measurements to a smaller set is comparatively higher than adding them to a greater set. The latter drawback is of particular importance when using greedy optimization

strategies along with different sets of information, as it might lead to suboptimal solutions far from the optimal one.[42] More recently, a framework based on the value of information that rigorously proposes a cost-benefit analysis for optimal sensor configuration has been reported in Cantero-Chinchilla et al,[1] where a trade-off between cost and information gain is provided whilst avoiding far from optimal solutions. Notwithstanding, although the aforementioned methodologies account for parameter uncertainties, these are usually limited to a specific set of updatable parameters (e.g., damage position coordinates). Other (nonupdatable) model parameters, such as stiffness, density, or wave speed, are usually regarded as constant input variables. However, these parameters are uncertain by nature and their uncertainties should be rigorously accounted for in a comprehensive robust methodology.

In recent years, the problem of optimization of sensors with nonupdatable parameter uncertainties has been explored by a number of researchers. Note that these parameters are not updated in a model-based inverse problem. In Argyris and Papadimitriou,[43] the expectation of the KL divergence (i.e., information gain) over the nonupdatable parameters was proposed as objective function, while the associated multidimensional integrals were addressed using asymptotic approximations. Using the same objective function, Papadimitriou[44] solved the multidimensional integrals analytically, given that a linear model of a *quantity of interest* (QoI) was available, except for the nonupdatable parameters which were approximated using Monte Carlo (MC) or grid sampling. In addition to the aforementioned expectation of the KL divergence, the objective function has also been robustly formulated by including the standard deviation of the KL with respect to the nonupdatable parameters in Ercan et al.[45] Nevertheless, there remains a need for a framework for optimal sensor placement considering nonlinear relations between the output QoI and the model parameters using the value of information as optimization criterion while avoiding biased results due to simplifications such as asymptotic approximations.

In this paper, a novel and robust methodology for optimal sensor configuration based on the value of information is proposed. This framework builds upon the work previously developed in Cantero-Chinchilla et al,[1] where a value of information-based approach for the optimization of SHM sensor configurations was proposed without accounting for uncertainties related to nonupdatable model parameters. Three major methodological contributions are provided in this paper:

(1) the uncertainty related to both updatable and nonupdatable model parameters is rigorously quantified here using information theoretic foundations and the value of information;
(2) the variability of the objective function with respect to the nonupdatable parameters for each candidate sensor location is quantified; and
(3) the spatial correlation between neighbor sensors [35] —assuming that nearby extra sensors add little information—is taken into account in the context of the value of information.

The proposed methodology is generic, but here, it is specialized for ultrasonic guided wave-based SHM for which uncertainties have demonstrated to play a significant role in the accuracy of damage diagnosis. Multiple sources of uncertainty are accounted for updatable and nonupdatable parameter uncertainties (e.g., uncertain material properties or damage characteristics), measurement and modeling error uncertainties, and value of information variability with respect to the nonupdatable parameters. In addition, this work comprehensively explores the influence of (1) modeling and experimental uncertainties and (2) the sensor optimization method by comparing the forward sequential sensor placement algorithm[46] based on a exhaustive search with the covariance matrix adaptation evolutionary strategy (CMA-ES)[47] (which has already proven effective for optimal sensor placement[48,49]). The results demonstrate the effectiveness of the proposed approach in providing robust optimal sensor configurations under modeling and measurement errors.

The remainder of this paper is organized as follows: Section 2 describes the value of information-based robust methodology for optimal sensor configuration and proposes an efficient algorithmic implementation for the objective function. Section 3 describes the chosen application on ultrasonic guided waves and illustrates the methodology throughout a number of case studies. In Section 4, a discussion is provided to comparatively explore the performance between optimization strategies; and finally, Section 5 provides concluding remarks.

2 | METHODOLOGY

2.1 | Robust objective function based on the expected value of information (EVI)

In this section, a robust objective function is proposed for the optimization of the number and location of a set of sensors. This function, based on the concept of the *value of information* and also on information theoretic principles,

measures the expected value added by a sensor configuration while trading-off information gain and cost. Further details on the mathematical derivation of the formulation of the optimal sensor configuration problem using the value of information are provided in Cantero-Chinchilla et al.[1] Mathematically, the EVI of a candidate sensor configuration $\mathcal{C}^n$ given a set of uncertain parameters $\boldsymbol{\xi} \in \Xi \in \mathbb{R}^{N_\xi}$ (e.g., model hypotheses such as wave propagation velocity or material density) whose inference is not required in the SHM problem can be defined as follows[1]:

$$\mathrm{EVI}(\boldsymbol{\xi}, \mathcal{C}^n) = f(n''_{opt}) \int_{\mathfrak{D}} \mathrm{KL}(p(\boldsymbol{\theta}|\mathbf{D}, \boldsymbol{\xi}, \mathcal{C}^n) \| p(\boldsymbol{\theta}|\boldsymbol{\xi}, \mathcal{C}^n)) p(\mathbf{D}) d\mathbf{D} - \underbrace{\alpha \cdot [f(n'_{opt}) - f(n''_{opt})]}_{\mathrm{RCI}}, \tag{1}$$

where $\mathbf{D} = \{\mathbf{y}(\mathcal{C}^n)\} \in \mathfrak{D} \in \mathbb{R}^{N_\mathbf{D}}$ denotes the available dataset in one damage scenario within the space of all possible measurements $\mathfrak{D}$ in all possible damage scenarios of a QoI (e.g., natural frequencies, mode shapes, or time of flight [ToF]) for an arbitrary sensor configuration $\mathcal{C}^n$; $f(n''_{opt})$ and $f(n'_{opt})$ are the cost saving functions, that is, stemming from an inverse of the cost function $f(n)$ of the optimal number of sensors (n''_{opt}) under posterior and prior information (n'_{opt}), respectively. The term $\mathrm{KL}(p(\boldsymbol{\theta}|\mathbf{D}, \boldsymbol{\xi}, \mathcal{C}^n) \| p(\boldsymbol{\theta}|\boldsymbol{\xi}, \mathcal{C}^n)) = \int_{\boldsymbol{\Theta}} \log[p(\boldsymbol{\theta}|\mathbf{D}, \boldsymbol{\xi}, \mathcal{C}^n)/p(\boldsymbol{\theta}|\boldsymbol{\xi}, \mathcal{C}^n)] p(\boldsymbol{\theta}|\mathbf{D}, \boldsymbol{\xi}, \mathcal{C}^n) d\boldsymbol{\theta}$ is the KL divergence between the prior $p(\boldsymbol{\theta}|\boldsymbol{\xi}, \mathcal{C}^n)$ and posterior $p(\boldsymbol{\theta}|\mathbf{D}, \boldsymbol{\xi}, \mathcal{C}^n)$ probability density functions (PDFs) of the set of updatable model parameters, namely, $\boldsymbol{\theta} \in \boldsymbol{\Theta} \in \mathbb{R}^{N_\theta}$; and finally, $\alpha > 0$ is a constant that establishes a weight to the relative cost of implementation (RCI). Both sets of parameters, that is, $\boldsymbol{\theta}$ and $\boldsymbol{\xi}$, constitute the input of a model $g(\boldsymbol{\theta}, \boldsymbol{\xi}, \mathcal{C}^n)$ of the QoI used to infer damage diagnosis information $\boldsymbol{\theta}$ (e.g., damage location). The inference considers certain mechanical properties contained in $\boldsymbol{\xi}$ (e.g., wave propagation velocity) and is done based on the data $\mathbf{D}$ acquired by the sensor configuration $\mathcal{C}^n$. In the SHM problem, the posterior $p(\boldsymbol{\theta}|\mathbf{D}, \boldsymbol{\xi}, \mathcal{C}^n)$ is obtained by updating the prior PDF $p(\boldsymbol{\theta}|\boldsymbol{\xi}, \mathcal{C}^n)$ using the data $\mathbf{D}$ and considering additional hypotheses about the value of $\boldsymbol{\xi}$. On the other hand, the optimal sensor configuration problem looks for the sensor layout $\mathcal{C}^n$ that maximizes the value of the information gained through its EVI.

Equation (1) is obtained by assuming a benefit function formed by a cost saving function along with the information gain between prior and posterior PDFs (refer to Cantero-Chinchilla et al[1] for further details). Note that the optimal design of the sensor configuration is conducted in a stage where the experimental data $\mathbf{D}$ are unavailable. Therefore, the posterior PDFs are treated as preposterior PDFs[50] depending on modeled data that stem from the likelihood function, rather than experimental data. Details on the formulation of the likelihood function and the stochastic embedding of a deterministic model about a QoI, are provided in Appendix A.

Notice that Equation (1) depends on a set of parameters $\boldsymbol{\xi}$ which are usually assumed as constants. These parameters may include physical properties of the system, prediction error quantities such as the standard deviations of the measurement and modeling errors ($\overline{\sigma}$ and $\tilde{\sigma}$, respectively), and the correlation length λ (refer to Appendix A). To provide a robust optimal configuration considering the uncertainties of $\boldsymbol{\xi}$, an expectation of the EVI with respect to $\boldsymbol{\xi}$, namely, $\mathbb{E}_{\boldsymbol{\xi}}[\mathrm{EVI}(\boldsymbol{\xi}, \mathcal{C}^n)]$, is formulated as follows:

$$\mathbb{E}_{\boldsymbol{\xi}}[\mathrm{EVI}(\boldsymbol{\xi}, \mathcal{C}^n)] = f(n''_{opt}) \int_{\Xi} \int_{\mathfrak{D}} \mathrm{KL}(p(\boldsymbol{\theta}|\mathbf{D}, \boldsymbol{\xi}, \mathcal{C}^n) \| p(\boldsymbol{\theta}|\boldsymbol{\xi}, \mathcal{C}^n)) p(\mathbf{D}) p(\boldsymbol{\xi}) d\mathbf{D} d\boldsymbol{\xi} - \mathrm{RCI}. \tag{2}$$

Note that the resulting equation involves multidimensional integrals that, in general, lack analytical solution; hence, approximation methods are required to obtain an estimate of the mathematical expectation. These may include MC or numerical integration methods, depending on the dimensionality of the sets of $\boldsymbol{\theta}$, $\mathbf{D}$, and $\boldsymbol{\xi}$.[1,51,52]

Note also that Equation (2) conveys the definition a robust estimator of the EVI with respect to $\boldsymbol{\xi}$. However, the resulting optimal configuration could still be prone to further variations of the EVI with respect to changes in the value of $\boldsymbol{\xi}$. To account for this variability and provide a further robust optimal sensor placement, the standard deviation of the $\mathrm{EVI}(\boldsymbol{\xi}, \mathcal{C}^n)$ is formulated as

$$\mathrm{Std}_{\boldsymbol{\xi}}[\mathrm{EVI}(\boldsymbol{\xi}, \mathcal{C}^n)] = \left[\int_{\Xi} \left(\mathrm{EVI}(\boldsymbol{\xi}, \mathcal{C}^n) - \mathbb{E}_{\boldsymbol{\xi}}[\mathrm{EVI}(\boldsymbol{\xi}, \mathcal{C}^n)] \right)^2 p(\boldsymbol{\xi}) d\boldsymbol{\xi} \right]^{1/2}. \tag{3}$$

Finally, by combining Equations (2) and (3), the robust objective (or utility) function for optimal sensor configuration $U(\mathcal{C}^n)$ is formulated as follows:

$$U(\mathcal{C}^n) = \mathbb{E}_{\boldsymbol{\xi}}[\mathrm{EVI}(\cdot)] - A \cdot \mathrm{Std}_{\boldsymbol{\xi}}[\mathrm{EVI}(\cdot)], \tag{4}$$

where $A > 0 \in \mathbb{R}^+$ is a constant that balances the importance of the EVI standard deviation within the utility function. Therefore, $U(\mathcal{C}^n)$ is considered here as the robust objective function that measures the utility of the candidate sensor configuration $\mathcal{C}^n$ considering uncertainties stemming from (1) preposterior parameters, (2) nonupdatable parameters,

and (3) the EVI. Observe that Equation (4) penalizes sensor configurations whose variability is high should the value of $\boldsymbol{\xi}$ change and establishes a trade-off between EVI and its variability. For example, if there are two candidate sensor configurations with same value of $\mathbb{E}_{\boldsymbol{\xi}}[\text{EVI}(\boldsymbol{\xi}, \mathcal{C}^n)]$, the proposed objective function will prioritize the one with smaller $\text{Std}_{\boldsymbol{\xi}}[\text{EVI}(\boldsymbol{\xi}, \mathcal{C}^n)]$, since it is more robust to variations in the values of the nonupdatable model parameters $\boldsymbol{\xi}$.

2.2 | Algorithmic implementation

The calculation of the objective function $U(\mathcal{C}^n)$ in Equation (4) involves three multidimensional integrals without trivial analytical solution. These integrals can be expressed, after the expansion of the KL divergence term (refer to Section 2.1) in Equation (2), as follows:

$$\mathbb{E}_{\boldsymbol{\xi}}[\text{EVI}(\boldsymbol{\xi},\mathcal{C}^n)] = f(n''_{opt}) \int_{\Xi}\int_{\mathfrak{D}}\int_{\boldsymbol{\theta}} \log\left[\frac{p(\boldsymbol{\theta}|\mathbf{D}, \boldsymbol{\xi}, \mathcal{C}^n)}{p(\boldsymbol{\theta}|\boldsymbol{\xi}, \mathcal{C}^n)}\right] p(\boldsymbol{\theta}|\mathbf{D},\boldsymbol{\xi},\mathcal{C}^n) p(\mathbf{D}) p(\boldsymbol{\xi}) d\boldsymbol{\theta} d\mathbf{D} d\boldsymbol{\xi} - \text{RCI}. \tag{5}$$

MC methods can be used to approximate each of the integrals of the Equation (5); however, the numerical approximation can be unstable unless significant amounts of samples are used.[53] As an alternative, integration methods such as the trapezoidal rule[54] are preferred since they can reach higher accuracy with a lower number of samples. The main limitation with numerical integration lies on the increasing dimensionality of the integral. Thus, in this work, a mixed rule is applied to compute the integrals with a numerical quadrature used when the dimension is no higher than two; otherwise, the MC integration is applied. Note that the standard deviation of the EVI (recall Equation 3) needs to be addressed after the expectation is obtained. Therefore, the samples used to estimate the expectation of the EVI can be reused to approximate the standard deviation, thus avoiding extra computational cost.

In this context, it is worth assessing the dimensionality of the variables that are integrated in Equation (5). In particular, the dimension of $\mathbf{D}$ equals the number of sensors considered in the candidate sensor configuration $\mathcal{C}^n$, which typically exceeds two. In this case, the integral of the KL divergence term over $\mathbf{D}$ is approximated using the Bayes' theorem, total probability theorem, and the MC method, based on the derivation proposed by Huan and Marzouk.[55] Conversely, the dimension of the other two variables, namely, $\boldsymbol{\theta}$ and $\boldsymbol{\xi}$, will depend on the complexity of the model used for inference. The aforementioned dimension-related rule applies for the estimation of their corresponding integrals, such that if $N_{\boldsymbol{\theta}} > 2$ and $N_{\boldsymbol{\xi}} > 2$, Equation (5) rewrites as[1,55]

$$\mathbb{E}_{\boldsymbol{\xi}}[\text{EVI}(\boldsymbol{\xi}, \mathcal{C}^n)] \approx \frac{f(n''_{opt})}{N^{\text{s}}_{\boldsymbol{\xi}}} \sum_{m=1}^{N^{\text{s}}_{\boldsymbol{\xi}}} \left[\frac{1}{N^{\text{s}}_{\mathbf{D}}} \sum_{j=1}^{N^{\text{s}}_{\mathbf{D}}} \sum_{i=1}^{N^{\text{s}}_{\boldsymbol{\theta}}} \left[\log p(y^{(i,j,m)}|\boldsymbol{\theta}^{(i)}, \boldsymbol{\xi}^{(m)}, \mathcal{C}^n) - \log\left(\sum_{k=1}^{N^{\text{s}}_{\boldsymbol{\theta}}} p(y^{(i,j,m)}|\boldsymbol{\theta}^{(k)}, \boldsymbol{\xi}^{(m)}, \mathcal{C}^n) \right) \right] \right] - \text{RCI}, \tag{6}$$

where $\boldsymbol{\theta}^{(i)}$ and $\boldsymbol{\xi}^{(m)}$ are samples drawn from the prior distribution $p(\boldsymbol{\theta}|\boldsymbol{\xi}, \mathcal{C}^n)$ and $p(\boldsymbol{\xi})$, respectively; and $y^{(i,j,m)}$ is a data sample drawn from the stochastic embedding of the deterministic model (see Appendix A) so that $y^{(i,j,m)} = g(\boldsymbol{\theta}^{(i)}, \boldsymbol{\xi}^{(m)}, \mathcal{C}^n) + \mathbf{e}^{(j)}(\mathcal{C}^n)$. Note that the samples of the prediction error $\mathbf{e}^{(j)}$ can be obtained as: $\mathbf{e}^{(j)} = \boldsymbol{0} + \boldsymbol{\Phi}\sqrt{\boldsymbol{\Lambda}}\omega^{(j)}$, where $\omega \sim \mathcal{N}(0,I)$, and $\boldsymbol{\Phi}$ and $\boldsymbol{\Lambda}$ are the eigenvector and diagonal eigenvalue matrices of the covariance matrix of $\mathbf{e}$ (i.e., $\boldsymbol{\Sigma}$). Alternatively, if $N_{\boldsymbol{\theta}} \leq 2$ and $N_{\boldsymbol{\xi}} \leq 2$, Equation (5) rewrites as

$$\mathbb{E}_{\boldsymbol{\xi}}[\text{EVI}(\boldsymbol{\xi},\mathcal{C}^n)] \approx f(n''_{opt}) \sum_{m=1}^{N^{\text{s}}_{\boldsymbol{\xi}}} w_m p(\boldsymbol{\xi}^{(m)}) \left[\frac{1}{N^{\text{s}}_{\mathbf{D}}} \sum_{j=1}^{N^{\text{s}}_{\mathbf{D}}} \sum_{i=1}^{N^{\text{s}}_{\boldsymbol{\theta}}} w_i p(\boldsymbol{\theta}^{(i)}) \left[\log p(y^{(i,j,m)}|\boldsymbol{\theta}^{(i)}, \boldsymbol{\xi}^{(m)}, \mathcal{C}^n) - \log\left(\sum_{k=1}^{N^{\text{s}}_{\boldsymbol{\theta}}} w_k p(\boldsymbol{\theta}^{(k)}) p(y^{(i,j,m)}|\boldsymbol{\theta}^{(k)}, \boldsymbol{\xi}^{(m)}, \mathcal{C}^n) \right) \right] \right] - \text{RCI}, \tag{7}$$

where w_m, w_i, and w_k are the coefficients used in the trapezoidal rule. Finally, note that if $N_{\boldsymbol{\theta}} \leq 2$ or $N_{\boldsymbol{\xi}} \leq 2$, then only its corresponding integral is approximated by the trapezoidal rule (this case is not shown in Algorithm 1). Therefore, the optimal sensor problem is defined by the maximization of the robust objective function as follows:

$$\begin{aligned} &\underset{n,\mathcal{C}}{\text{maximize}} \quad U(\mathcal{C}^n) = \mathbb{E}_{\boldsymbol{\xi}}[\text{EVI}(\cdot)] - A \cdot \text{Std}_{\boldsymbol{\xi}}[\text{EVI}(\cdot)] \\ &\text{subject to} n \leq N_s. \end{aligned} \tag{8}$$

Observe from the last equation that the main constraint is that the number of sensors n for a given configuration should be less or equal than the maximum number of sensors (N_s). Additional constraints can be introduced related to the position of the sensor location, for example, the sensors are placed within the area of the structure. However, these constraints are case specific, and they are not formulated in Equation (8).

The optimization is addressed using a forward sequential sensor search.[46] Here, two strategies are considered for the identification of the optimal location of the nth sensor: (1) the CMA-ES,[47] in cases where the objective function $U(\mathcal{C}^n)$ is computationally heavy, and (2) an exhaustive search over a discrete grid of the $n_{s,max}$ possible sensor locations. The CMA-ES algorithm is a state-of-the-art stochastic optimization algorithm adopted in this paper due to its efficiency in solving optimization problems with computationally expensive and complex utility functions. The algorithm aims to identify adaptively the probability distribution of the optimal system parameters. It assumes a Gaussian probability distribution and uses the sequentially available optimization data in order to construct its mean and covariance matrix. The algorithm has been shown to require less number of function evaluations than other optimization algorithms in several benchmark problems and applications.[47] This makes CMA-ES particularly suitable to maximize the objective function (Equation 8) due to its high computational cost. Besides, its stochastic nature allows dealing with noisy cost functions. A pseudoalgorithm of the proposed methodology is provided in Algorithm 1 considering both strategies for the search of the optimal sensor location and the different integration methods (i.e., MC and the trapezoidal rule). Note that the optimal design is dependent on uncertainties associated with the updatable and nonupdatable parameters as well as the experimental and modeling errors ($\overline{\sigma}$ and $\tilde{\sigma}$), which are defined using prior or engineering knowledge.

Algorithm 1: Pseudo-code implementation of forward sequential search algorithm for geometrically unconstrained sensor configurations.

// If N_θ & $N_\xi > 2$
// Preamble:
Set $\bar{\sigma}$ and $\tilde{\sigma}$ // Appendix A;
Define $p(\boldsymbol{\theta})$ and $p(\boldsymbol{\xi})$;
Define N_s;
Define $n_{s,max}$;
// Algorithm:
Obtain $n'_{opt} \leftarrow \arg\max_n f(n)$;
Obtain $\{\boldsymbol{\theta}^{(i)}\}_{i=1}^{N_\theta^s} \sim p(\boldsymbol{\theta})$;
Obtain $\{\mathbf{e}^{(j)}\}_{j=1}^{N_\mathbf{D}^s} \sim \mathcal{N}(0, I)$;
Obtain $\{\boldsymbol{\xi}^{(m)}\}_{m=1}^{N_\xi^s} \sim p(\boldsymbol{\xi})$;
// Forward sequential sensor search:
$\mathbf{C} \leftarrow \emptyset$;
for $n = 1$ **to** N_s **do**
  // Search algorithm: (1) or (2)
  // (1) CMA-ES:
  Obtain $\mathcal{C}^n_{\text{opt}} \leftarrow \arg\max U(\mathcal{C}^n)$ // Equations (4), (6), and (3) using CMA-ES;
  Store $\mathbf{C} \leftarrow \mathbf{C} \cup \mathcal{C}^n_{\text{opt}}$;
  // (2) Exhaustive search:
  for $i = 1$ **to** $n_{s,max}$ **do**
    $\mathcal{C}^n \leftarrow \mathcal{C}^{n-1} \cup \mathcal{C}^i$;
    Obtain $\mathbb{E}_\xi[\text{EVI}(\boldsymbol{\xi}, \mathcal{C}^n)]$ // Equation (6);
    Obtain $\text{Std}_\xi[\text{EVI}(\boldsymbol{\xi}, \mathcal{C}^n)]$ // Equation (3);
    Obtain $U(\mathcal{C}^n)$ // Equation (4);
  end
  Obtain $\mathcal{C}^n_{\text{opt}} \leftarrow \arg\max U(\mathcal{C}^n)$;
  Store $\mathbf{C} \leftarrow \mathbf{C} \cup \mathcal{C}^n_{\text{opt}}$;
end
Obtain $n''_{\text{opt}} \leftarrow \arg\max U(\mathbf{C})$;

// If N_θ & $N_\xi \leq 2$
// Preamble:
Set $\bar{\sigma}$ and $\tilde{\sigma}$ // Appendix A;
Define $p(\boldsymbol{\theta})$ and $p(\boldsymbol{\xi})$;
Define N_s;
Define $n_{s,max}$;
// Algorithm:
Obtain $n'_{opt} \leftarrow \arg\max_n f(n)$;
Obtain $\{\boldsymbol{\theta}^{(i)}\}_{i=1}^{N_\theta^s}$ // from a grid;
$\{\mathbf{e}^{(j)}\}_{j=1}^{N_\mathbf{D}^s} \sim \mathcal{N}(0, I)$;
Obtain $\{\boldsymbol{\xi}^{(m)}\}_{m=1}^{N_\xi^s}$ // from a grid;
// Forward sequential sensor search:
$\mathbf{C} \leftarrow \emptyset$;
for $n = 1$ **to** N_s **do**
  // Search algorithm: (1) or (2)
  // (1) CMA-ES:
  Obtain $\mathcal{C}^n_{\text{opt}} \leftarrow \arg\max U(\mathcal{C}^n)$ // Equations (4), (7), and (3) using CMA-ES;
  Store $\mathbf{C} \leftarrow \mathbf{C} \cup \mathcal{C}^n_{\text{opt}}$;
  // (2) Exhaustive search:
  for $i = 1$ **to** $n_{s,max}$ **do**
    $\mathcal{C}^n \leftarrow \mathcal{C}^{n-1} \cup \mathcal{C}^i$;
    Obtain $\mathbb{E}_\xi[\text{EVI}(\boldsymbol{\xi}, \mathcal{C}^n)]$ // Equation (7);
    Obtain $\text{Std}_\xi[\text{EVI}(\boldsymbol{\xi}, \mathcal{C}^n)]$ // Equation (3);
    Obtain $U(\mathcal{C}^n)$ // Equation (4);
  end
  Obtain $\mathcal{C}^n_{\text{opt}} \leftarrow \arg\max U(\mathcal{C}^n)$;
  Store $\mathbf{C} \leftarrow \mathbf{C} \cup \mathcal{C}^n_{\text{opt}}$;
end
Obtain $n''_{\text{opt}} \leftarrow \arg\max U(\mathbf{C})$;

We emphasize that the maximization of the objective function (Equation 8) requires the use of the same samples either from a PDF or a grid, depending on the approximation method, for every candidate sensor configuration

$\mathcal{C}^n$.[31,51,56] This prevents the objective function from becoming stochastic, which would happen if different samples were used for every function evaluation, thus enabling the identification of a reliable optimum. Note also that the forward sequential sensor search algorithm reduces the computational complexity for relatively high number of sensors,[46] which would be intractable should an exhaustive combinatorial optimization strategy be adopted.

3 | VALIDATION FOR ULTRASONIC GUIDED WAVE-BASED DAMAGE LOCALIZATION

The proposed methodology is generic but here it is applied to the optimization of piezoelectric sensor configurations of an ultrasonic guided wave-based SHM system for damage localization. The monitored structure is a 500 mm× 400 mm aluminum plate with 1.5 mm thickness. Damage is assumed to exist at any location within a specified area of the plate, thus the damage coordinates comprise the set of updatable parameters (which would be inferred in a model-based inverse problem) in this example. Note that single events of damage are considered only since these initial stages of damage is what can be expected in reality in maintenance-intensive industries. Additional physics-based variables, which are usually assumed to be uncertain, are considered here with quantified uncertainty as nonupdatable parameters. These variables encompass the frequency of excitation or the mechanical properties of the plate (both directly affecting the wave propagation velocity).

The problem of damage localization is addressed here by a model-based Bayesian inverse problem using an ellipse-based ToF model,[57] which was previously published in Cantero-Chinchilla et al.[58] The ToF can be obtained as the difference between the time to obtain the first energy peak of the excitation signal and the one from the scattered signal. In mathematical terms, the ToF information of the scattered signals for a particular actuator-sensor pair is defined as follows[59]:

$$\mathrm{ToF}^{(a-s)} = \frac{\sqrt{(X_d - X_a)^2 + (Y_d - Y_a)^2}}{V_{a-d}} + \frac{\sqrt{(X_d - X_s)^2 + (Y_d - Y_s)^2}}{V_{d-s}}, \tag{9}$$

where $(X_d, Y_d) \in \mathbb{R}^2$ are the coordinates of the damage position, $(X_a, Y_a) \in \mathbb{R}^2$ are the actuator transducer coordinates, $(X_s, Y_s) \in \mathbb{R}^2$ are the coordinates of one particular sensor, and V_{a-d} and V_{d-s} are the wave propagation velocities of the actuator–damage and damage–sensor paths, respectively. Note that for isotropic materials, the velocity is independent on the wave propagation direction, hence $V = V_{a-d} = V_{d-s}$. We note that the ellipse is formed by the two foci actuator and sensor and passes through the damage position. Thus, such an ellipse represents all the points of the plate with same ToF, since the sum of distances between the foci and any point in the curve is constant. When additional sensors are added to the system, the intersection between ellipses provides the most probable damage location.

The robust optimal sensor configuration is addressed using the ToF model in Equation (9) to generate the datasets $\mathbf{D}$ for the optimization process.* The damage coordinates $\boldsymbol{\theta} = \{X_d, Y_d\}$ are the updatable model parameters whereas the wave propagation velocity V is a nonupdatable (or nuisance) uncertain parameter, thus $\boldsymbol{\xi} = \{V\}$. The uncertainty about of the wave velocity is assumed to be given by a Gaussian PDF, thus $V \sim \mathcal{N}(2800, 40^2)$ with units expressed in m/s. Note that this velocity corresponds to the first antisymmetric wave mode at 300 kHz in an aluminum alloy 2024. Furthermore, damage may occur at any point within a closed designated area with the same probability. Note also that since the dimensionality of both set of parameters is less than or equal to two, their corresponding integrals are computed with the trapezoidal rule (refer to Equation 7 and Algorithm 1). For illustration purposes, the inverse of the cost function $f(n)$ is chosen here as a decreasing monotonic function,[1] as $f(n) = 100/(n^2 + 100)$; the constant A (Equation 4) is assumed to be $A = 3$; and α (Equation 1) is considered as $\alpha = 1$. The definition of inverse of the cost function $f(n)$ is case specific and depends on multiple factors: the manufacturing processes of the sensors, how they are installed and maintained, data acquisition costs, among others. Different features of the proposed robust methodology are investigated in the following subsection.

3.1 | Effect of the prediction errors on the optimal sensor placement

The effect of the two prediction error terms considered in the stochastic embedding process (see Appendix A) are assessed by analyzing their influence in the optimal sensor placement for the first sensor. To this end, the number of samples considered for the numerical integrals in Equation (7) are $N_{\boldsymbol{\theta}}^{\mathrm{s}} = 4$, $N_{\mathbf{D}}^{\mathrm{s}} = 300$, and $N_{\boldsymbol{\xi}}^{\mathrm{s}} = 21$. The samples for $\mathbf{D}$

*Note that the $\mathrm{ToF}^{(a-s)}$ in Equation (9) corresponds to the term $g(\boldsymbol{\theta}, \boldsymbol{\xi}, \mathcal{C}^n)$ in Equation (A1) of Appendix A.

are used within the MC approximation, while those from $\boldsymbol{\theta}$ and $\boldsymbol{\xi}$ are adopted for the trapezoidal rule. In this example, a small area of damage, represented by $N_{\boldsymbol{\theta}}^{s} = 4$ grid samples, is considered in order to provide more insight into the sensor placement and the effect of model and measurement errors. An exhaustive sensor search approach is adopted here over a grid of $n_{s,max} = 4141$ possible sensor locations with coordinates $X_s \in \{0{,}0.005{,}...{,}0.5\}$ and $Y_s \in \{-0.2, -0.019{,}...{,}0.2\}$ in meters. The actuator is assumed to be placed at two locations, one at a time, that is, (0.35 m, 0.16 m) and (0.15 m, −0.05 m) in (X_a, Y_a) coordinate pairs.

First, we show the geometrical aspects of the ToF (or ellipse-based) model as a consequence of a sensor configuration based on information gain. To facilitate the understanding of this relation, a very low value for the measurement error is adopted, that is, $\overline{\sigma} = 1\text{e-}9$ s, while the actuator is placed at (0.35 m, 0.16 m). With this low-error scenario, the best and worst sensor locations (given by the maximum and minimum value of $U(\mathcal{C}^1)$, respectively) are almost entirely provided by model-related aspects. Indeed, if we focus on a low-informative sensor location (e.g., along the blue dashed lines in Figure 1) and draw the four ellipses formed by the foci pair actuator–sensor that pass through the four samples in the damage area (i.e., each corner of the blue rectangle), we notice that at least two of the ellipses overlap—green ellipses in Figure 1. As these two ellipses are unable to differentiate between the two damage locations, the information gain is lower than in any other case where ellipses do not overlap, in which case would produce higher information gain and lower evidence (refer to Appendix B.1).

Next, the effect of the measurement error in the optimal sensor placement is investigated. The optimal location for the first sensor $\mathcal{C}^1_{\text{opt}}$ and its corresponding objective function value $U(\mathcal{C}^1)$ are shown in Figure 2 for different values of the measurement error $\overline{\sigma} \in \{1\text{e-}7, 1\text{e-}6, 1\text{e-}5, 1\text{e-}4, 1\text{e-}3\}$ with units in seconds, neglecting the modeling error contribution, that is, $\tilde{\sigma} = 0$. Note that the optimal sensor placements for the lowest level of noise $\overline{\sigma} = 1\text{e-}7$ s show a uniform gray area where the objective function is maximized (see Figure 2a,c). In these cases, the sensor could be placed anywhere within this region while providing the optimal value of $U(\mathcal{C}^1)$. This result is qualitatively repeated even when the actuator location varies (see Figure 2c), which means that for very accurate sensors and measurement equipment (i.e., low $\overline{\sigma}$ values), the optimal sensor location may not be unique and that it is related to geometrical aspects stemming from the ellipse-based model. When $\overline{\sigma}$ increases, that is, by increasing measurement error, the optimal placement tends to collapse to a single point for higher values of $\overline{\sigma}$ (see Figure 2a,c and refer to Appendix B for additional details). This optimal location is placed farther from the damage area (i.e., at the edge of the plate) in the same side of the actuator. The increased distance between the optimal sensor location and the damage area is related to the magnitude of both the ToF and $\overline{\sigma}$. We conclude that the farther the sensor is placed from the damage, the higher the ToF prediction and the less influence from the measurement error is obtained on the stochastic embedding (Equation A1).

Furthermore, the EVIs for each of the previous optimal solutions with respect to $\overline{\sigma}$ are analyzed. These are depicted in Figure 2b,d for both alternative actuator locations. It can be observed that $U(\mathcal{C}^1)$ sharply decreases between $\overline{\sigma}$ values of 1e-6 s and 1e-5 s, tending to a horizontal asymptote for higher values of $\overline{\sigma}$ as there is a negligible level of information gain. This happens when the values of the modeling error are similar in magnitude to the ToF model predictions. Note that for both actuators, the ToF predictions lie in the interval [5.68e-05,2.65e-04] s, depending on the sensor location

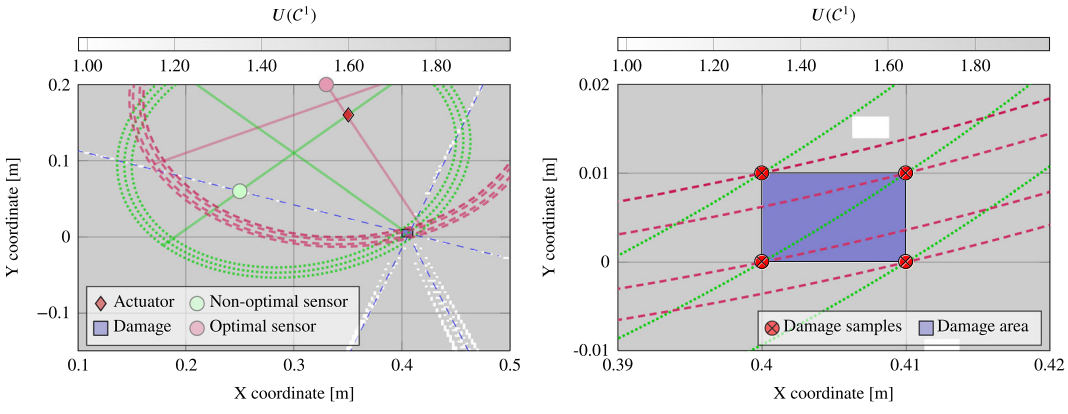

(a) Optimal sensor placement – Actuator (0.35m, 0.16m)

(b) Zoom view of (a)

FIGURE 1 Optimal sensor placement for $\overline{\sigma} = 1\text{e-}9$ s represented as gray areas. Blue dashed lines represent least informative sensor locations. Examples of best and worst ellipses (purple and green dashed lines, respectively) considering optimal and nonoptimal sensor locations, are also shown

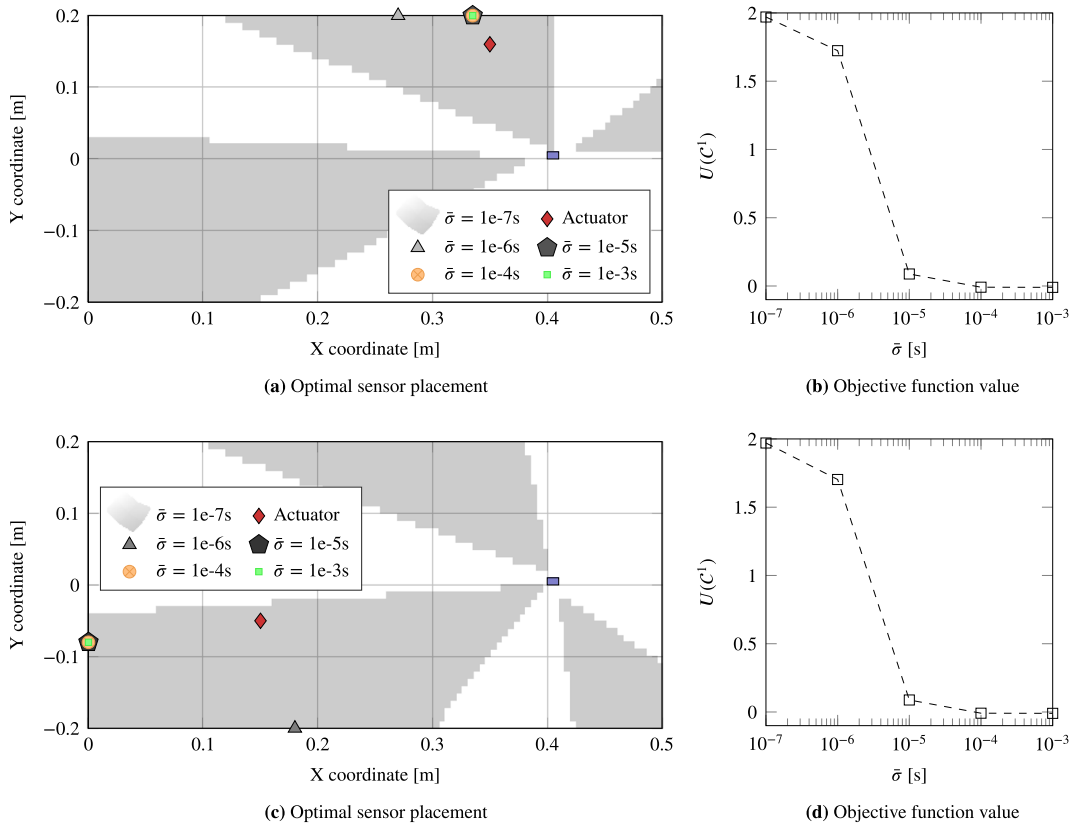

(a) Optimal sensor placement **(b)** Objective function value

(c) Optimal sensor placement **(d)** Objective function value

FIGURE 2 (a) Optimal sensor placement for the first sensor ($\mathcal{C}^1$) with regard to several values of $\overline{\sigma} > 0$ s assuming $\tilde{\sigma} = 0$ and the actuator at (0.35 m, 0.16 m). (b) The objective function value with respect to $\overline{\sigma}$. (c,d) Analogous results for a different actuator location at (0.15 m, −0.05 m). Area of possible damage occurrence is represented as a blue rectangle

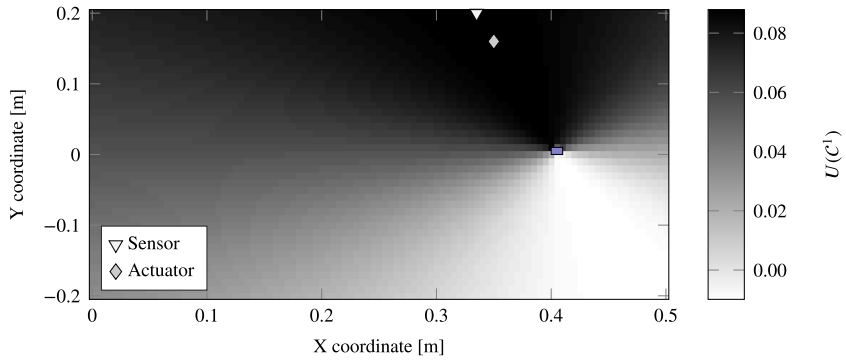

FIGURE 3 Map of the objective function using the exhaustive search of the first sensor location for the case of $\overline{\sigma} = 1\text{e-}5$ s, $\tilde{\sigma} = 0$, and the actuator at (0.35 m, 0.16 m)

and the value of V. Therefore, when $\overline{\sigma}$ is higher or of the same order of magnitude as the model predictions, the uncertainty of the preposterior PDFs is relatively high, and hence, the optimal sensor placement provides very low information.

We remark that the sensors are repeatedly optimally placed in the same side of the plate as the actuator. In fact, the opposite side (with respect to the damage) becomes the least informative location, as shown in Figure 3. Notice that the optimal sensor location is the one that provides the highest information gain, which, from an information theoretic perspective (whereby the information gain equals the difference between goodness-of-fit and evidence[60]), means that the optimal location has either a better fitness with the data or provides the lowest evidence. Given that the fitness to the data is relatively similar for any sensor location, then we can assert that it is the evidence the reason of such a high information gain, which takes the smallest value at the most informative location.

A sensitivity study is carried out by assuming the modeling error term as $\tilde{\sigma} = 0.05$ s with a correlation length $\lambda = 0.02$ m (see Appendix A). The results in Figure 4 show that the optimal sensor location depends on the modeling error term, being located nearby of the damage area for low values of $\overline{\sigma}$, that is, 1e-7 s, 1e-6 s, and 1e-5 s. When $\overline{\sigma} = 1\text{e-}4$ s, the optimal sensor location lies somewhere between the actuator and the damage area. In the case of $\overline{\sigma} = 1\text{e-}3$ s, the sensor is placed at a boundary coinciding with the case previously shown in Figure 2. The shape of $U(\mathcal{C}^1)$ with respect to $\overline{\sigma}$ shows, in Figure 4b,d, a similar trend to the curves obtained for $\tilde{\sigma} = 0$ in Figure 2.

The results of this sensitivity investigation suggest that a trade-off between the measurement and modeling error terms is taking place, which dictates the optimal position of the sensor. Note that the error covariance is assumed to be defined by a combination of (1) a measurement error term that remains constant, that is, $\mathbf{\Sigma}_{\mathcal{D}} = \overline{\sigma}^2\mathbf{I}$, and (2) a modeling error term that is dependent on the model prediction and whose $k\ell$th element of its covariance matrix is given by $\Sigma_{\mathcal{M}}^{k\ell} = \tilde{\sigma}^2 g_k g_\ell \exp(-|\mathbf{x}^k - \mathbf{x}^\ell|/\lambda)$ (refer to Appendix A). When $\tilde{\sigma} = 0$ and $\overline{\sigma} > 0$ s, the information gain is maximized for a sensor placed at a location far from the damage, since the magnitude of the model prediction g is considerably larger than the $\overline{\sigma} > 0$ s, as observed in Figure 2. However, when $\tilde{\sigma}$ is nonzero and constant, and $\overline{\sigma} > 0$ s, several scenarios may appear:

- The influence of $\tilde{\sigma}$ is greater than $\overline{\sigma}$ in the optimal sensor placement. In this case, the modeling error, which is proportional the ToF model (Equation 9), is minimized when the sensor is very close to the damage as the magnitude of the model prediction is the smallest. Thus, the information gain is maximized, and the optimal sensor is placed nearby of the damage area. This behavior can be observed in Figure 4 for a measurement error of $\overline{\sigma} \in [1\text{e-}7, 1\text{e-}5]$ s and modeling error of $\tilde{\sigma} = 0.05$ with $\lambda = 0.02$ m.
- The influence of $\tilde{\sigma}$ is smaller than $\overline{\sigma}$ in the optimal sensor placement. In this scenario, the measurement error term is predominant and therefore sensor locations that provide higher values of the ToF will be preferred, as previously discussed. This is evident from the results shown in Figure 2 (with $\overline{\sigma} > 0$ s and $\tilde{\sigma} = 0$) given that the sensors are located relatively far from the damage area.

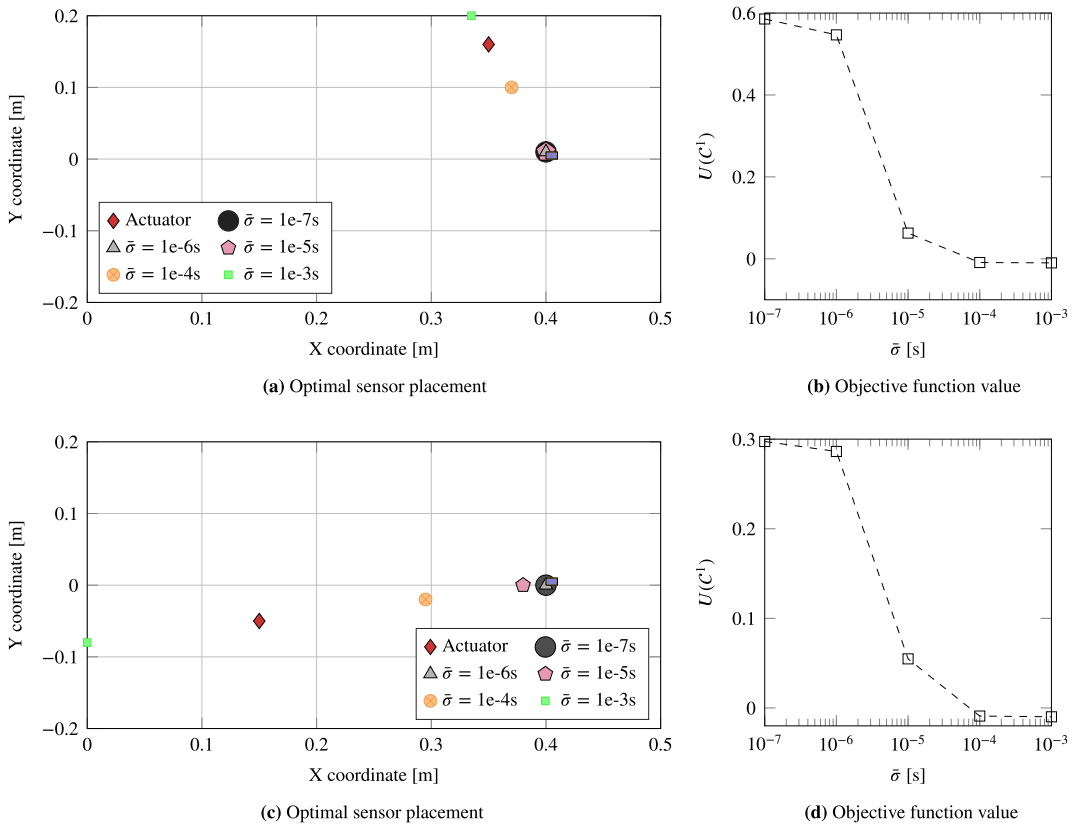

(a) Optimal sensor placement **(b)** Objective function value

(c) Optimal sensor placement **(d)** Objective function value

FIGURE 4 (a) Optimal sensor placement for the first sensor ($\mathcal{C}^1$) with regard to several values of $\overline{\sigma} > 0$ assuming $\tilde{\sigma} = 0.05$, $\lambda = 0.02$ m, and the actuator at (0.35 m, 0.16 m). (b) The objective function value with respect to $\overline{\sigma}$. (c,d) Analogous results for a different actuator location at (0.15 m, −0.05 m). Area of possible damage occurrence is represented as a blue rectangle

- The influence of $\tilde{\sigma}$ is similar to $\overline{\sigma}$ in the optimal sensor placement. A balance takes place in this case and the optimal sensor location is found to be neither in the nearby of the damage nor the boundary of the plate but at in an intermediate point. This is observed in Figure 4 for $\overline{\sigma} = 1\text{e-}4$ s and $\tilde{\sigma} = 0.05$ with $\lambda = 0.02$ m.

In this context, the importance of choosing an appropriate value for both error terms has been revealed. An inadequate value of $\tilde{\sigma}$ or $\overline{\sigma}$ could lead to a biased optimal sensor location and an over or under estimation of the EVI. These results suggest that in practice, with larger modeling errors due to modeling simplifications, the sensors should be placed as close as possible to the area of possible damage occurrence. On the other hand, when the accuracy of the model is relatively high, cheaper sensors with less quality can be chosen and placed at a farther location from the damage area.

4 | DISCUSSION

4.1 | Performance comparison between optimization strategies

A comparison of the chosen sensor placement strategies using the CMA-ES and the exhaustive search is addressed in this section for different actuator locations and several values of both measurement and modeling error terms. Figure 5d shows the results for an actuator placed at (0.35 m, 0.16 m) using two values of the prediction error terms, namely, (1) $\overline{\sigma} = 1\text{e-}6$ s and $\tilde{\sigma} = 0$, shown in Figure 5a,b, and (2) $\overline{\sigma} = 1\text{e-}6$ s, $\tilde{\sigma} = 5\text{e-}4$, and $\lambda = 0.02$ m in Figure 5c,d. For the case of (1), Figure 5a reveals that both optimization strategies provide similar sensor placements. The slight sensor placement variations stem from the capability of CMA-ES to deal with continuous variables, while the exhaustive search is based on a grid of discrete sensor locations. Note that the absence of correlation in the modeling error (recall that $\tilde{\sigma} = 0$) makes the fourth and fifth sensors locations to coincide in the plate, which manifests the sensor clustering effect

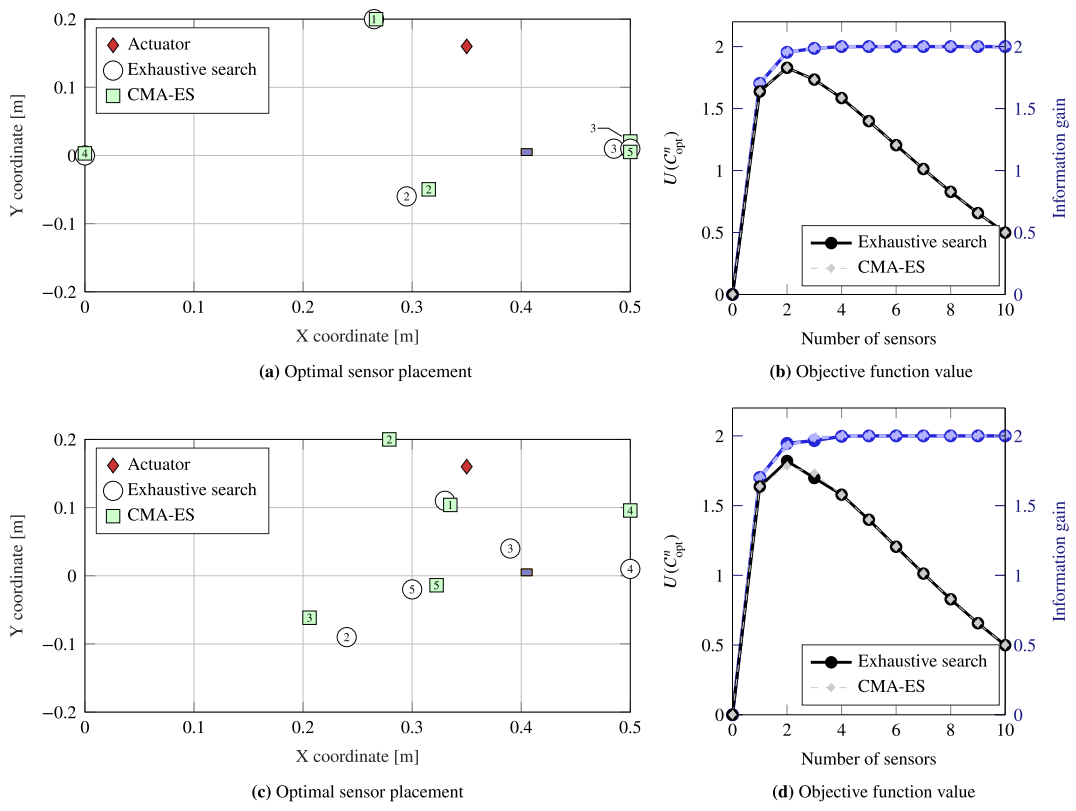

(a) Optimal sensor placement

(b) Objective function value

(c) Optimal sensor placement

(d) Objective function value

FIGURE 5 (a) Comparison of exhaustive search and CMA-ES through the optimal sensor placement for five sensors ($\mathcal{C}^5$) with $\overline{\sigma} = 1\text{e-}6$ s, $\tilde{\sigma} = 0$, and the actuator at (0.35 m, 0.16 m). The number inside the markers represents the order of sensor selection. (b) The objective function (gray scale) in comparison with the information gain (blue scale). (c,d) Analogous results for $\tilde{\sigma} = 5\text{e-}4$. The blue rectangle represents the damage area

already discussed in Papadimitriou and Lombaert.[35] The values of the objective function are also very similar for the two strategies as depicted in Figure 5b. For the case of (2), the resulting sensor distributions are different from (1), as shown in Figure 5c, which also shows that the optimal location varies depending on the search algorithm. This is caused by the appearance of several local (and near-global) maxima in the objective function because of the addition of the modeling error term. This makes the CMA-ES to focus on local maxima and find suboptimal locations compared to the exhaustive search. However, notice that both the information gain and objective function values are very similar for both configurations. This similarity suggests that the CMA-ES only provides one of the multiple near-global solutions, which is almost identical to the one provided by the exhaustive search.

To further investigate the large difference in the optimal location of the second sensor, Figure 6 is provided to show a map of the objective function values obtained when the exhaustive search is used. The optimal location of the first sensor is provided from the initial step in the forward sequential sensor search algorithm. Besides, we observe that there are three separate areas with relatively similar values of $U(\mathcal{C}^2)$ (represented by similar gray tones), which causes the CMA-ES to find a local optimum in one of them since they share similar objective function values.

Also, by comparing the information curves, we find that the first sensor is the most informative. From the second sensor onward, the relative information gain is relatively small, which causes the sensor placement to be less sensitive. Additionally, it is worth highlighting that the optimal sensor locations are highly sensitive to the value of $\tilde{\sigma}$. Even when introducing a relatively small value of $\tilde{\sigma} = 0.05\%$, the optimal sensor layout is considerably affected. In this case, both the information gain and the objective function curves are slightly smaller when introducing $\tilde{\sigma} > 0$. This is caused by increment in uncertainty in the model error, which causes a smaller information gain about the damage localization. In summary, CMA-ES provides near-optimal sensor configurations that are almost equally informative to the ones found by the exhaustive search. Note that for the optimization of SHM systems, the designer usually seeks near-most informative and valuable configurations that are far from the worst scenarios, and in this context, both the CMA-ES and exhaustive search strategies have been successful.

The computational efficiency of both optimization approaches is relatively similar. The chosen plate dimensions and grid of possible sensor locations, with a resolution in the X coordinate of 0.005 m and 0.01 m for Y, results in 4141 candidate locations that are evaluated with the objective function in the exhaustive search. This number is maintained at every stage of the forward sequential sensor search algorithm. The CMA-ES shows a higher efficiency with a number of function evaluations that varies between 300 and 1500 depending on the chosen tolerances. However, the CMA-ES needs to be repeated several times due to its stochastic nature specially when multiple local minima appears in the objective function, thus reducing its apparent computational advantage. Nonetheless, the CMA-ES would be a preferred method in cases where the possible number of sensor locations is very large, making the exhaustive search strategy unfeasible.

4.2 | Optimal sensor placement over a greater area of damage

In engineering practice, the optimal sensor placement is usually addressed for a larger area of possible damage occurrence. To show the behavior of the optimal sensor layout in such a scenario, the area of damage is now considered as a

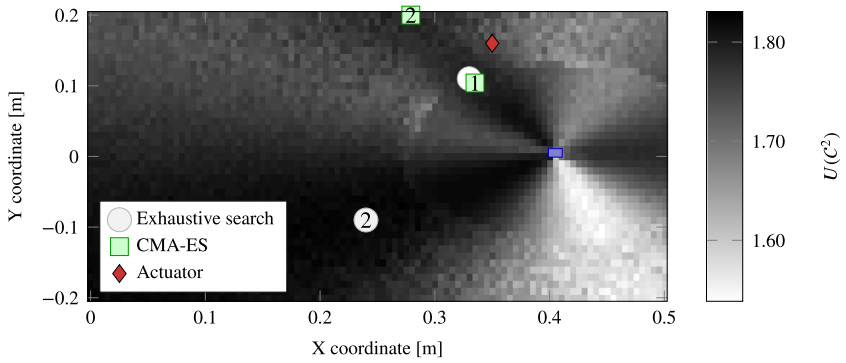

FIGURE 6 Map of the objective function using the exhaustive search for the second sensor location using $\overline{\sigma} = 1\text{e-}6$ s, $\tilde{\sigma} = 5\text{e-}4$. The actuator, in red diamond, is placed at (0.35 m, 0.16 m)

rectangle from (0.3 m, −0.1 m) to (0.5 m, 0.1 m) with the actuator being placed at (0.15 m, −0.05 m), as shown in Figure 7a. The number of samples used for the numerical integrals remain the same except for the updatable parameters $\boldsymbol{\theta}$, which is increased to $N_{\boldsymbol{\theta}}^{s} = 121$. The samples are uniformly distributed over the rectangular area. The measurement error part is assumed to be $\overline{\sigma} =$ 1e-6 s while the modeling error is defined by $\tilde{\sigma} = 0.05$ and $\lambda = 0.02$ m. The optimal sensor locations are expected to be close to the area of damage, according to Section 3.1. In this section, the relative position with respect to the area of damage (e.g., inside or at the boundary) is investigated.

Figure 7 depicts the resulting optimal sensor layouts obtained by applying both the exhaustive search and CMA-ES. The optimal number of sensors under the robust value of information criterion is found to be $n''_{\text{opt}} = 3$ as observed in Figure 7b, and their corresponding layouts are shown in Figure 7a. It is worth highlighting that both algorithms provide very similar objective function values and sensor layouts. This is revealed clearly in the information gain curve shown in Figure 7b, since each additional sensor provides a relatively high amount of information. Compared to the previous case of a very small damage area, a higher number of sensors is now required to fully recover the maximum amount of information that the data can provide. Then, there is no clear optimal number of sensors from the amount of information criterion alone. Conversely, the value of information renders a clear maximum stemming from the concave curve in Figure 7b. Notice that the sensors are placed at the boundary of the area of damage, except for the first one, which is placed slightly within such an area.

In order to provide more insight into the optimal sensor placement, Figure 7c shows the objective function in the exhaustive search of the third optimal sensor location. We observe that given the correlation part of the modeling error, the areas that surround the two previous optimal sensor locations are penalized in the utility function to avoid sensor clustering and they hold the minimum utility values. The third sensor is then placed at the bottom part of the area of damage. Note that the coincidence of optimal placement for both sensor search approaches is partially due to the absence of local maxima in the objective function (as observed for a small area of damage in Figure 6), thus making it easier for the CMA-ES to identify the global optimum.

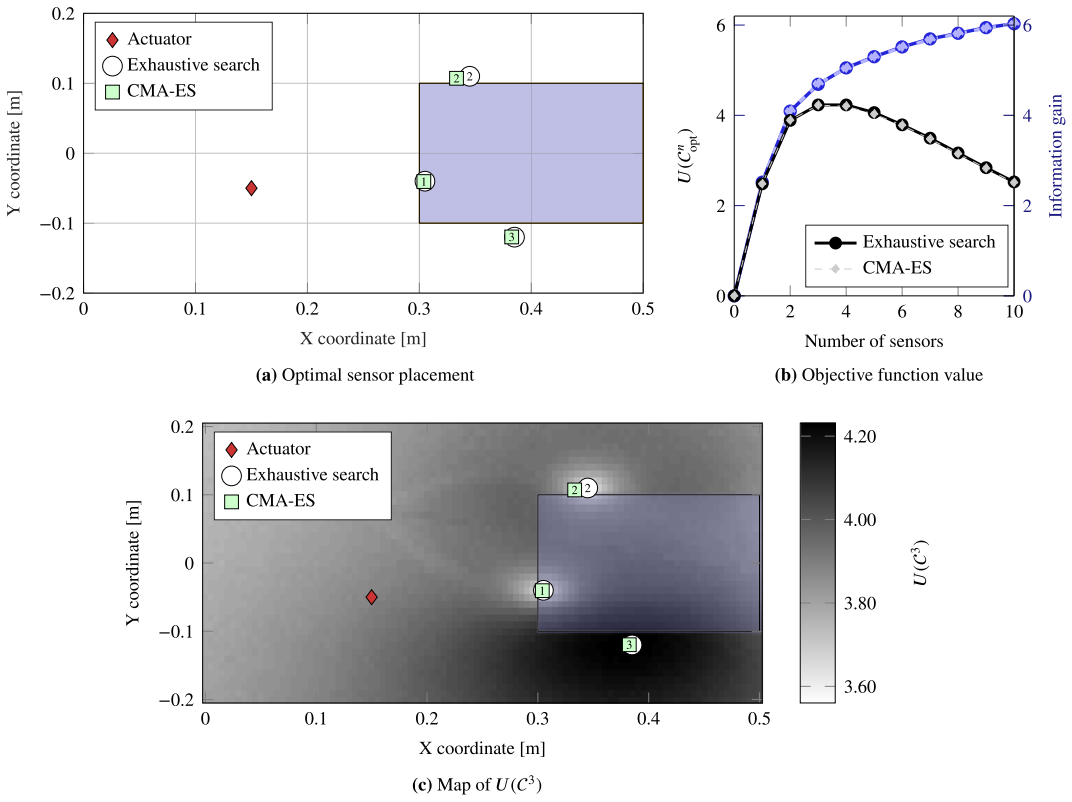

(a) Optimal sensor placement

(b) Objective function value

(c) Map of $U(C^3)$

FIGURE 7 (a) Optimal sensor placement obtained for a greater area of possible damage occurrence using the exhaustive search and CMA-ES, (b) comparison between value and amount of information, and (c) map of $U(\mathcal{C}^3)$

4.3 | Effectiveness of the optimal sensor layout

The effectiveness of the optimal sensor configuration is demonstrated by showing the dispersion of the damage reconstruction of one sample within the possible area of damage with respect to three sensor distributions. To this end, we consider the optimal sensor layout obtained in Section 4.2 with $U(\mathcal{C}^3_{\text{opt}}) = 4.2312$ and two additional suboptimal layouts with utility $U(\mathcal{C}^3) = 3.1860$ and $U(\mathcal{C}^3) = 2.6317$. These distributions are represented by circles, squares, and pentagons, respectively, and are shown in Figure 8a. The damage sample is assumed to be at (0.4 cm, 0 cm), and it is reconstructed using the Bayesian damage localization approach proposed in Cantero-Chinchilla et al.[58] The posterior distributions of the damage coordinates for the chosen sensor layouts are shown in Figure 8b–d. Observe that the information provided by the optimal configuration is more accurate than the suboptimal ones, hence highlighting the importance of optimizing any SHM system in the design stage to obtain accurate and robust results.

4.4 | On the comparison with other techniques

This paper has introduced a novel methodology for robust optimal sensor configuration of SHM systems based on the value of information criterion. The approach is based on a previous paper,[1] where the optimal sensor placement was addressed using the EVI, but presents the following significant novel and key properties with respect to the EVI formulation in Cantero-Chinchilla et al.[1]: (1) It is able to quantify uncertainties related to nuisance parameters $\boldsymbol{\xi}$; (2) the utility function allows the quantification of the variability of the EVI due to to the uncertainty of the nuisance parameters $\boldsymbol{\xi}$ at each candidate sensor location through the standard deviation of the EVI, which penalizes designs highly sensitive to changes in the value of $\boldsymbol{\xi}$; and (3) the method considers the spatial correlation error between multiple sensors, hence avoiding sensor clustering (as shown in Figures 5 and 7c). These points make the proposed methodology more immune to uncertainties compared to Cantero-Chinchilla et al,[1] thus providing more robust sensor configurations.

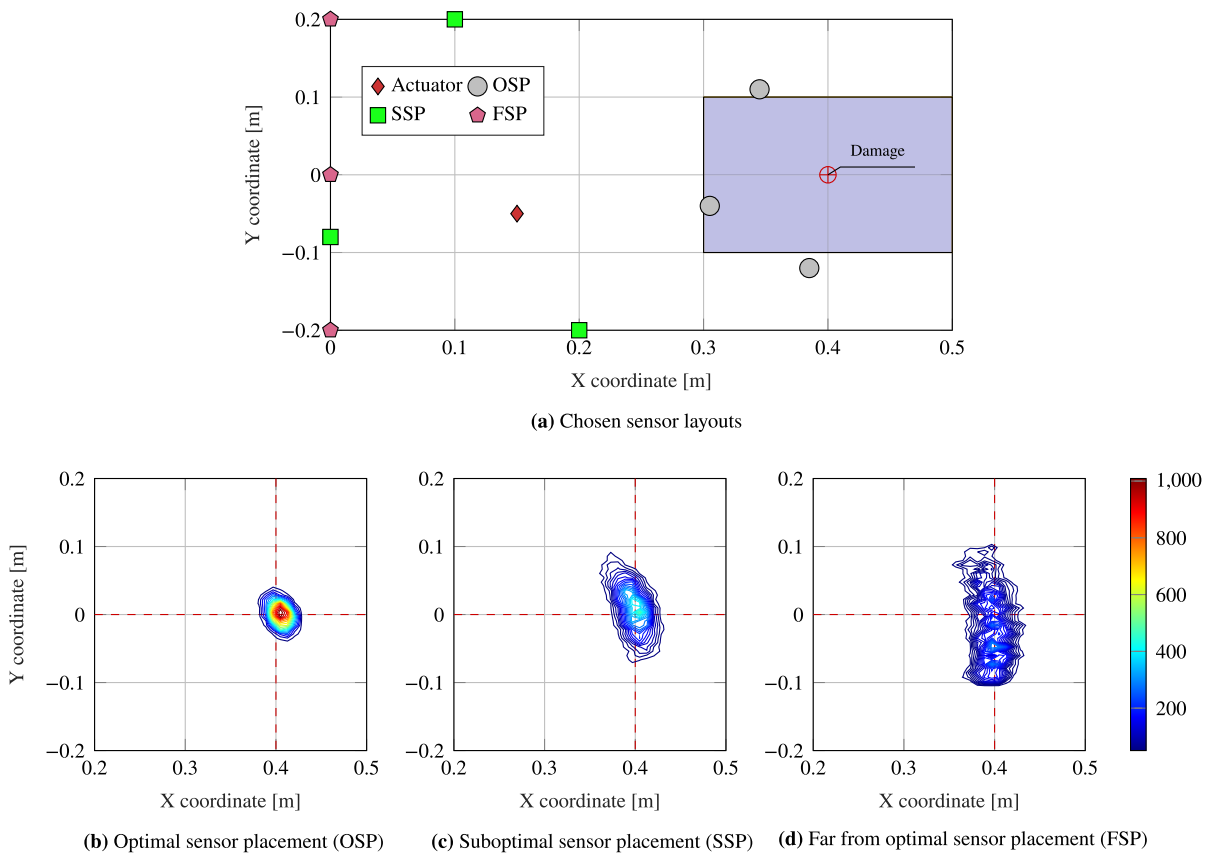

(a) Chosen sensor layouts

(b) Optimal sensor placement (OSP) **(c)** Suboptimal sensor placement (SSP) **(d)** Far from optimal sensor placement (FSP)

FIGURE 8 (a) Geometrical distribution of the three sensor layouts and (b–d) their corresponding damage reconstruction. The color bar represents the probability density

The aforementioned features have an effect on the optimal location and number of sensors, as shown in Figure 9 for a direct comparison against Cantero-Chinchilla et al[1] under the assumptions made in Section 4.2. Note that the nonrobust EVI formulation in Cantero-Chinchilla et al[1] provides the optimal design with sensors at the boundary of the plate, while the proposed robust EVI methodology locate them close to the area of damage. This difference is principally caused by the assumption made about the modeling error ($\tilde{\sigma} = 0.05$ and $\lambda = 0.02$ m), which was not present in Cantero-Chinchilla et al.[1] (equivalent to $\tilde{\sigma} = 0$). Both designs are obtained using the exhaustive search for the sake of simplicity and to not introduce further variability in the solution. Note also that the optimal number of sensors (two for the nonrobust formulation and three for the robust one) and the value of the objective function result to be different for the two approaches. This comparison manifests the importance of considering most sources of uncertainty present in the optimal sensor placement problem, namely, updatable and nonupdatable parameter uncertainties, measurement and modeling error uncertainties, and EVI variability with respect to the nonupdatable parameters.

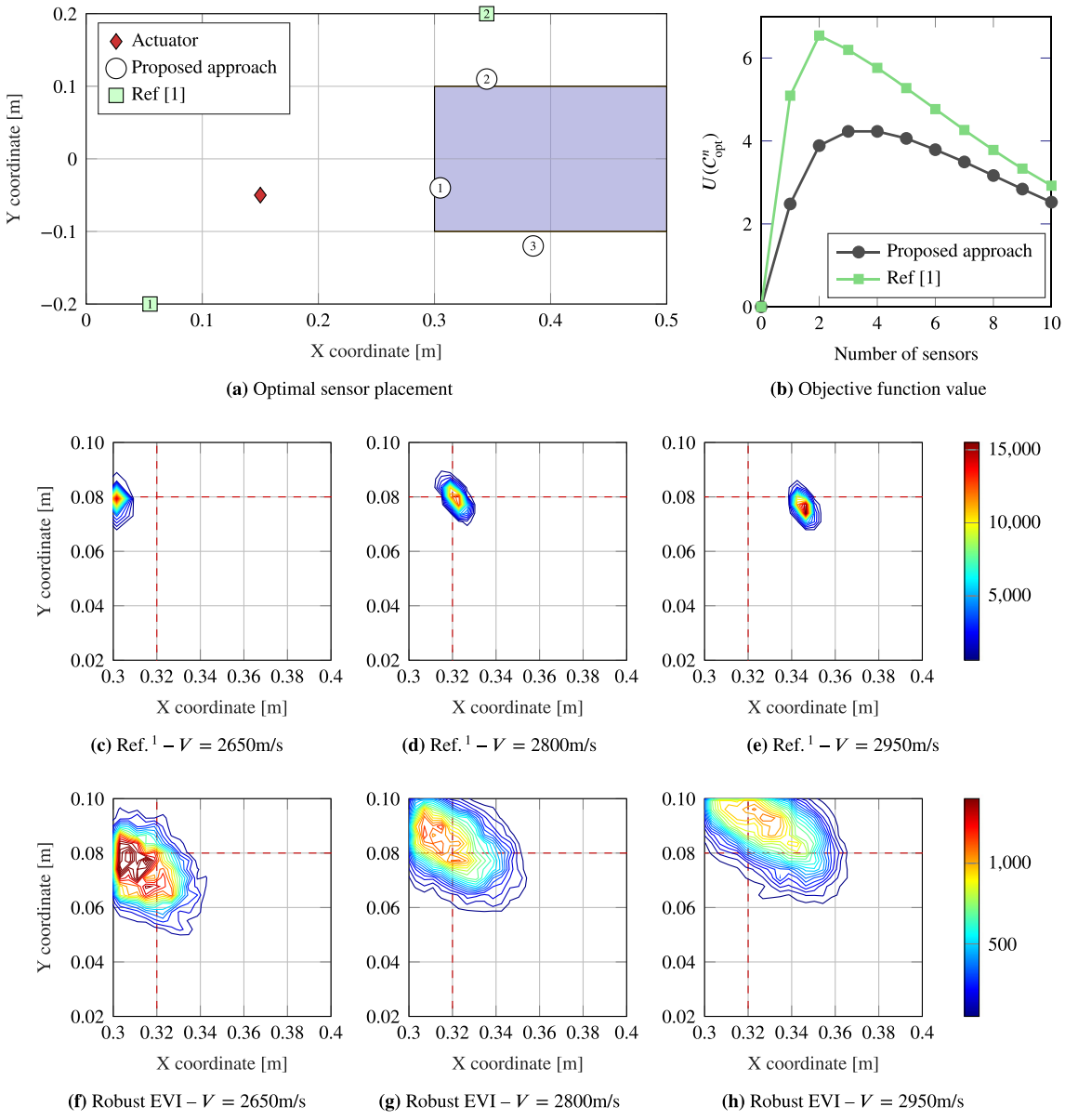

(a) Optimal sensor placement **(b)** Objective function value

(c) Ref.[1] – $V = 2650$m/s **(d)** Ref.[1] – $V = 2800$m/s **(e)** Ref.[1] – $V = 2950$m/s

(f) Robust EVI – $V = 2650$m/s **(g)** Robust EVI – $V = 2800$m/s **(h)** Robust EVI – $V = 2950$m/s

FIGURE 9 (a,b) Optimal sensor placement and objective function value obtained with the proposed robust methodology and using the one in Cantero-Chinchilla et al.[1] Damage reconstruction with different values of the nuisance parameter V using (c–e) the optimal EVI criterion Cantero-Chinchilla et al[1] and (f–h) the robust EVI criterion. True parameters: $X_d = 0.32$ m, $Y_d = 0.08$ m, and $V = 2800$ m/s. The color bar represents the probability density

In terms of damage reconstruction, the robust optimal solution provides a larger area of possible damage occurrence, which makes it more robust against changes or errors in the nuisance (or nonupdatable) parameter. A simulated damage is considered to be located at $X_d = 0.32\,\text{m}$, $Y_d = 0.08\,\text{m}$ for the aluminum plate with a true wave propagation velocity of $V = 2800\,\text{m/s}$. Three cases are addressed by using the optimal designs obtained by the proposed robust methodology and Cantero-Chinchilla et al.[1] (refer to Figure 9a) with different nuisance parameter values: the true wave velocity and a $\pm 5\%$ variation. Figure 9c–h shows that the sensor layout given by Cantero-Chinchilla et al[1] is more sensitive to possible errors in the nuisance parameter and fails to localize the damage using erroneous velocity values. The robust sensor placement provides a posterior PDF that is always overlapping with the true damage location. This example illustrates the advantages of accounting for uncertainties of the nuisance parameters in the optimal design of SHM systems.

5 | CONCLUSIONS

We present a robust framework for identifying optimal sensor configurations using the value of information. This framework takes into account the uncertainty of the updatable model parameters in an inverse problem, as well as the uncertainty related to the nonupdatable parameters (e.g., physical properties of the system). We investigated two alternatives for computing the integrals associated with the robust objective function: numerical quadrature and MC approximation. Additionally, two sensor search strategies are compared: the exhaustive search over a grid of possible sensor locations and an evolution strategy (the CMA-ES). The proposed method is validated for ultrasonic guided wave-based damage localization and the following conclusions are drawn:

- There exists a trade-off between measurement noise and modeling error in the optimal sensor placement, which suggests that (1) when the modeling error is relatively high, the sensors should be optimally placed near the damage area, and (2) when the measurement error is predominant, the sensors are to be placed farther away from the damage area.
- The sensors are optimally placed at the boundary of the damage area when a relatively high value of the modeling error is considered.
- The identification of damage location for three different sensor configurations, from the optimal one to subsequently worse suboptimal configurations, has revealed the importance and effectiveness of optimizing SHM systems with the appropriate modeling of the uncertainty.
- The robust optimal sensor layout is more immune to potential errors on the assumption of these nuisance parameter values.
- The CMA-ES as an optimal sensor search algorithm is proven to be almost as effective and in any case more efficient than the exhaustive search. When a number of multiple near-global solutions may exist, the CMA-ES can provide a different optimal sensor configuration from the one provided by the exhaustive search. Nonetheless, these different configurations correspond to almost identical objective values and hence near-optimal sensor configurations.

ACKNOWLEDGMENTS

This paper is part of the SAFE-FLY project that has received funding from the European Union's Horizon 2020 Research and Innovation Programme under the Marie Skłodowska-Curie (Grant Agreement No. 721455). The authors acknowledge the support acquired by the Brazilian National Council of Research CNPq (Grant Agreement ID: 314168/2020-6).

AUTHOR CONTRIBUTIONS

Sergio Cantero-Chinchilla: Conceptualization, formal analysis, investigation, methodology, software, validation, visualization, writing - original draft preparation. **Costas Papadimitriou:** Conceptualization, methodology, supervision, writing - review & editing. **Juan Chiachío:** Conceptualization, methodology, writing - review & editing. **Manuel Chiachío:** Conceptualization, methodology, writing - review & editing. **Petros Koumoutsakos:** Supervision, writing - review & editing. **Adriano T. Fabro:** Funding acquisition, writing - review & editing. **Dimitrios Chronopoulos:** Funding acquisition, project administration, writing - review & editing.

DATA AVAILABILITY STATEMENT

The data that support the findings of this study are available from the corresponding author upon reasonable request.

REFERENCES

1. Cantero-Chinchilla S, Chiachío J, Chiachío M, Chronopoulos D, Jones A. Optimal sensor configuration for ultrasonic guided-wave inspection based on value of information. *Mech Syst Signal Process*. 2020;135:106377.
2. Guratzsch RF, Mahadevan S. Structural health monitoring sensor placement optimization under uncertainty. *AIAA J*. 2010;48(7):1281-1289.
3. Flynn EB, Todd MD. A Bayesian approach to optimal sensor placement for structural health monitoring with application to active sensing. *Mech Syst Signal Process*. 2010;24(4):891-903.
4. Li D, Ho S-CM, Song G, Ren L, Li H. A review of damage detection methods for wind turbine blades. *Smart Mater Struct*. 2015;24(3):033001.
5. Jang K, Kim N, An Y-K. Deep learning–based autonomous concrete crack evaluation through hybrid image scanning. *Struct Health Monit*. 2018;18(5–6):1722-1737.
6. Doebling SW, Farrar CR, Prime MB, et al. A summary review of vibration-based damage identification methods. *Shock Vib Dig*. 1998;30(2):91-105.
7. Behnia A, Chai HK, Shiotani T. Advanced structural health monitoring of concrete structures with the aid of acoustic emission. *Constr Build Mater*. 2014;65:282-302.
8. Annamdas VGM, Soh CK. Application of electromechanical impedance technique for engineering structures: review and future issues. *J Intell Mater Syst Struct*. 2010;21(1):41-59.
9. Giurgiutiu V. Tuned Lamb wave excitation and detection with piezoelectric wafer active sensors for structural health monitoring. *J Intell Mater Syst Struct*. 2005;16(4):291-305.
10. Chillara VK. A thermodynamic approach to nonlinear ultrasonics for material state awareness and prognosis. *Contin Mech Thermodyn*. 2017;29(6):1291-1311.
11. Barke D, Chiu WK. Structural health monitoring in the railway industry: a review. *Struct Health Monit*. 2005;4(1):81-93.
12. Su Z, Ye L, Lu Y. Guided Lamb waves for identification of damage in composite structures: a review. *J Sound Vib*. 2006;295(3-5):753-780.
13. Mitra M, Gopalakrishnan S. Guided wave based structural health monitoring: a review. *Smart Mater Struct*. 2016;25(5):053001.
14. Willberg C, Duczek S, Vivar-Perez JM, Ahmad ZAB. Simulation methods for guided wave-based structural health monitoring: a review. *Appl Mech Rev*. 2015;67(1):010803.
15. Thierry V, Brown L, Chronopoulos D. Multi-scale wave propagation modelling for two-dimensional periodic textile composites. *Compos Part B: Eng*. 2018;150:144-156.
16. Croxford AJ, Moll J, Wilcox PD, Michaels JE. Efficient temperature compensation strategies for guided wave structural health monitoring. *Ultrasonics*. 2010;50(4-5):517-528.
17. Wilcox P, Castaings M, Monkhouse R, Cawley P, Lowe M. An example of the use of interdigital PVDF transducers to generate and receive a high order Lamb wave mode in a pipe. *Review of Progress in Quantitative Nondestructive Evaluation*. Springer; 1997:919-926.
18. Worden K, Burrows AP. Optimal sensor placement for fault detection. *Eng Struct*. 2001;23(8):885-901.
19. Mallardo V, Aliabadi MH, Khodaei ZS. Optimal sensor positioning for impact localization in smart composite panels. *J Intell Mater Syst Struct*. 2013;24(5):559-573.
20. Ostachowicz W, Soman R, Malinowski P. Optimization of sensor placement for structural health monitoring: a review. *Struct Health Monit*. 2019;18(3):963-988.
21. Thiene M, Khodaei ZS, Aliabadi MH. Optimal sensor placement for maximum area coverage (MAC) for damage localization in composite structures. *Smart Mater Struct*. 2016;25(9):095037.
22. Khodaei ZS, Aliabadi MH. An optimization strategy for best sensor placement for damage detection and localization in complex composite structures. In: 8th European Workshop on Structural Health Monitoring (EWSHM 2016). UPV-EHU; 2016:5-8.
23. Salmanpour MS, Sharif Khodaei Z, Aliabadi MH. Transducer placement optimisation scheme for a delay and sum damage detection algorithm. *Struct Control Health Monit*. 2017;24(4):e1898.
24. Soman R, Kudela P, Balasubramaniam K, Singh SK, Malinowski P. A study of sensor placement optimization problem for guided wave-based damage detection. *Sensors*. 2019;19(8):1856.
25. Staszewski WJ, Worden K, Wardle R, Tomlinson GR. Fail-safe sensor distributions for impact detection in composite materials. *Smart Mater Struct*. 2000;9(3):298.
26. Lin FYS, Chiu P-L. A near-optimal sensor placement algorithm to achieve complete coverage-discrimination in sensor networks. *IEEE Commun Lett*. 2005;9(1):43-45.
27. Blanloeuil P, Nurhazli NE, Veidt M. Particle swarm optimization for optimal sensor placement in ultrasonic SHM systems. In: Nondestructive Characterization and Monitoring of Advanced Materials, Aerospace, and Civil Infrastructure 2016, Vol. 9804. International Society for Optics and Photonics; 2016:98-108.
28. Gao H, Rose JL. Ultrasonic sensor placement optimization in structural health monitoring using evolutionary strategy. In: AIP Conference Proceedings, Vol. 820. American Institute of Physics; 2006:1687-1693.
29. Markmiller JFC, Chang F-K. Sensor network optimization for a passive sensing impact detection technique. *Struct Health Monit*. 2010;9(1):25-39.
30. Ewald V, Groves R, Benedictus R. Integrative approach for transducer positioning optimization for ultrasonic structural health monitoring for the detection of deterministic and probabilistic damage location. *Struct Health Monit*. 2021;20(3):1117-1144.
31. Argyris C, Chowdhury S, Zabel V, Papadimitriou C. Bayesian optimal sensor placement for crack identification in structures using strain measurements. *Struct Control Health Monit*. 2018;25(5):e2137.

32. Capellari G, Chatzi E, Mariani S. Structural health monitoring sensor network optimization through Bayesian experimental design. *ASCE-ASME J Risk Uncertain Eng Syst Part A: Civ Eng*. 2018;4(2):04018016.
33. Beck JL, Papadimitriou C, Au S-K, Vanik MW. Entropy-based optimal sensor location for structural damage detection. In: Smart Structures and Materials 1998: Smart Systems for Bridges, Structures, and Highways, Vol. 3325. International Society for Optics and Photonics; 1998:161-173.
34. Papadimitriou C, Beck JL, Au S-K. Entropy-based optimal sensor location for structural model updating. *J Vib Control*. 2000;6(5):781-800.
35. Papadimitriou C, Lombaert G. The effect of prediction error correlation on optimal sensor placement in structural dynamics. *Mech Syst Signal Process*. 2012;28:105-127.
36. Argyris C. Bayesian uncertainty quantification and optimal experimental design in data driven simulations of engineering systems. *Ph. D. Thesis*: University of Thessaly; 2017.
37. Bhattacharyya P, Beck J. Exploiting convexification for Bayesian optimal sensor placement by maximization of mutual information. *Struct Control Health Monit*. 2020;27(10):e2605.
38. Cantero-Chinchilla S, Beck JL, Chiachío M, Chiachío J, Chronopoulos D, Jones A. Optimal sensor and actuator placement for structural health monitoring via an efficient convex cost-benefit optimization. *Mech Syst Signal Process*. 2020;144:106901.
39. Straub D. Value of information analysis with structural reliability methods. *Struct Saf*. 2014;49:75-85.
40. Faber MH, Thöns S. On the value of structural health monitoring. In: 22nd Conference on European Safety and Reliability. CRC Press; 2014:2535-2544.
41. Malings C, Pozzi M. Value of information for spatially distributed systems: Application to sensor placement. *Reliab Eng Syst Safety*. 2016;154:219-233.
42. Malings C, Pozzi M. Submodularity issues in value-of-information-based sensor placement. *Reliab Eng Syst Safety*. 2019;183:93-103.
43. Argyris C, Papadimitriou C. Bayesian optimal experimental design using asymptotic approximations. *Model Validation and Uncertainty Quantification*, Vol. 3. Springer; 2017:273-275.
44. Papadimitriou C. Optimal sensor placement for response reconstruction in structural dynamics. *Model Validation and uncertainty Quantification*, Vol. 3. Springer; 2020:205-210.
45. Ercan T, Koumoutsakos P, Papadimitriou C. *Robust Bayesian Optimal Sensor Placement for Model Parameter Estimation and Response Predictions*: European Association for Structural Dynamics; 2020.
46. Papadimitriou C. Optimal sensor placement methodology for parametric identification of structural systems. *J Sound Vib*. 2004;278(4-5):923-947.
47. Hansen N, Müller SD, Koumoutsakos P. Reducing the time complexity of the derandomized evolution strategy with covariance matrix adaptation (CMA-ES). *Evol Comput*. 2003;11(1):1-18.
48. Soman R, Ostachowicz W. Ultrasonic fiber Bragg grating sensor placement optimization in structural health monitoring using covariance matrix adaptation evolutionary strategy. In: Health Monitoring of Structural and Biological Systems XV, Vol. 11593. International Society for Optics and Photonics; 2021:327-334.
49. Tan Y, Zhang L. Computational methodologies for optimal sensor placement in structural health monitoring: a review. *Struct Health Monit*. 2020;19(4):1287-1308.
50. Konakli K, Faber MH. Value of information analysis in structural safety. In: Beer M, ed. *Vulnerability, Uncertainty, and Risk: Quantification, Mitigation, and Management*: University of Liverpool. American Society of Civil Engineers; 2014:1605-1614. Second International Conference on Vulnerability and Risk Analysis and Management (ICVRAM 2014).
51. Verma S, Papadimitriou C, Lüthen N, Arampatzis G, Koumoutsakos P. Optimal sensor placement for artificial swimmers. *J Fluid Mech*. 2020;884:A24.
52. Ryan KJ. Estimating expected information gains for experimental designs with application to the random fatigue-limit model. *J Comput Graph Stat*. 2003;12(3):585-603.
53. Smyth GK. *Numerical Integration*: Wiley StatsRef: Statistics Reference Online; 2014.
54. Bathe K-J. *Finite Element Procedures*: Klaus-Jurgen Bathe; 2006.
55. Huan X, Marzouk YM. Simulation-based optimal Bayesian experimental design for nonlinear systems. *J Comput Phys*. 2013;232(1):288-317.
56. Huan X, Marzouk Y. Gradient-based stochastic optimization methods in Bayesian experimental design. *Int J Uncertain Quantif*. 2014;4(6):479-510.
57. Flynn EB, Todd MD, Wilcox PD, Drinkwater BW, Croxford AJ. Maximum-likelihood estimation of damage location in guided-wave structural health monitoring. *Proc R Soc A Math Phys Eng Sci*. 2011;467(2133):2575-2596.
58. Cantero-Chinchilla S, Chiachío J, Chiachío M, Chronopoulos D, Jones A. A robust Bayesian methodology for damage localization in plate-like structures using ultrasonic guided-waves. *Mech Syst Signal Process*. 2019;122:192-205.
59. Ihn J-B, Chang F-K. Pitch-catch active sensing methods in structural health monitoring for aircraft structures. *Struct Health Monit*. 2008;7(1):5-19.
60. Beck JL. Bayesian system identification based on probability logic. *Struct Control Health Monit*. 2010;17(7):825-847.

How to cite this article: Cantero-Chinchilla S, Papadimitriou C, Chiachío J, et al. Robust optimal sensor configuration using the value of information. *Struct Control Health Monit*. 2022;29(12):e3143. doi:10.1002/stc.3143

APPENDIX A: STOCHASTIC EMBEDDING OF THE DETERMINISTIC MODEL

We assume a deterministic model $g(\boldsymbol{\theta}, \boldsymbol{\xi}, \mathcal{C}^n)$ that provides predictions of a QoI, for which a dataset $\mathbf{y}(\mathcal{C}^n) \in \mathbb{R}^{N_\mathbf{D}}$ is available for an arbitrary sensor configuration $\mathcal{C}^n$ of n sensors. The model $g(\boldsymbol{\theta}, \boldsymbol{\xi}, \mathcal{C}^n)$ depends on both a set of uncertain parameters $\boldsymbol{\theta} \in \boldsymbol{\Theta} \in \mathbb{R}^{N_\theta}$, which are subsequently estimated in a Bayesian inverse problem framework, and also on a set of uncertain parameters $\boldsymbol{\xi} \in \boldsymbol{\Xi} \in \mathbb{R}^{N_\xi}$ that are assumed to be deterministic (i.e., constant). Given that the model is just a representation of the reality, a certain degree of discrepancy between the model predictions and the measurements will appear, so

$$\mathbf{y}(\mathcal{C}^n) = g(\boldsymbol{\theta},\boldsymbol{\xi},\mathcal{C}^n) + \mathbf{e}(\mathcal{C}^n), \tag{A1}$$

where $\mathbf{e}(\mathcal{C}^n)$ is the set of prediction model errors, which are assumed to be represented by a multivariate Gaussian distribution with zero-mean and a covariance matrix $\boldsymbol{\Sigma}(\boldsymbol{\sigma})$, so $\mathbf{e} \sim \mathcal{N}(\boldsymbol{0},\boldsymbol{\Sigma})$. This covariance matrix can be separated into two independent sources of error[35]: (1) the modeling error $\boldsymbol{\Sigma}_\mathcal{M}$ and (2) the measurement error $\boldsymbol{\Sigma}_\mathcal{D}$, thus: $\boldsymbol{\Sigma} = \boldsymbol{\Sigma}_\mathcal{M} + \boldsymbol{\Sigma}_\mathcal{D}$. Given the stochastic independence between measurement errors and sensor locations, the covariance matrix of the measurement error can be defined as follows: $\boldsymbol{\Sigma}_\mathcal{D} = \overline{\sigma}^2\mathbf{I}$, where $\mathbf{I}$ denotes the identity matrix and $\overline{\sigma}$ is its standard deviation. On the other hand, the covariance matrix of the modeling error $\boldsymbol{\Sigma}_\mathcal{M}$ is assumed here to be spatially correlated with regard to the sensors location to avoid sensor clustering and its $k\ell$th position is given by

$$\Sigma^{k\ell}_\mathcal{M} = \sqrt{\Sigma^{kk}_\mathcal{M}\Sigma^{\ell\ell}_\mathcal{M}}R(\eta^{k\ell}), \tag{A2}$$

where $R(\eta^{k\ell})$ is the spatial correlation structure and is selected to be exponential as follows:

$$R(\eta^{k\ell}) = \exp\left(-\frac{|\mathbf{x}^k - \mathbf{x}^\ell|}{\lambda}\right), \tag{A3}$$

where $\mathbf{x}^k$ is the coordinates of the kth sensor position and λ is a measure of the spatial correlation length. In addition, the variance $\Sigma^{kk}_\mathcal{M}$ of the model prediction error at the kth sensor location is defined by $\Sigma^{kk}_\mathcal{M} = \tilde{\sigma}^2 g^2_k(\boldsymbol{\theta}, \boldsymbol{\xi}, \mathcal{C}^n)$, which represents the dependence of the covariance of the modeling error on the intensity of the model output, where $\tilde{\sigma}$ is the standard deviation of the modeling error normalized by such intensity. In this context, the probabilistic description of the prediction error, that is, the likelihood function $p(\mathbf{y}|\boldsymbol{\theta}, \boldsymbol{\xi}, \mathcal{C}^n)$, is defined as follows:

$$p(\mathbf{y}|\boldsymbol{\theta}, \boldsymbol{\xi}, \mathcal{C}^n) = \frac{1}{\left(\sqrt{2\pi}\right)^n\sqrt{\det\,\boldsymbol{\Sigma}(\boldsymbol{\sigma})}}\exp\left(-\frac{1}{2}[\mathbf{y}(\mathcal{C}^n) - g(\boldsymbol{\theta},\ \boldsymbol{\xi},\ \mathcal{C}^n)]^T\boldsymbol{\Sigma}(\boldsymbol{\sigma})^{-1}[\mathbf{y}(\mathcal{C}^n) - g(\boldsymbol{\theta},\ \boldsymbol{\xi},\ \mathcal{C}^n)]\right). \tag{A4}$$

This function provides an estimate of the discrepancy between the data and model predictions.

APPENDIX B: RELATIONSHIP BETWEEN ToF MODEL, INFORMATION GAIN, AND OPTIMAL SENSOR LOCATION

B.1 | Low value of the measurement error

To demonstrate the results shown in Figure 1 (with $\overline{\sigma} = 1\text{e-}9\,\text{s}$ and $\tilde{\sigma} = 0$), we assume only one sample for the nuisance parameter $N_\xi = 1$ along with a single data sample $N_\mathbf{D} = 1$, which allows Equation (7) to be simplified as follows:

$$\mathbb{E}_{\boldsymbol{\xi}}[\mathrm{EVI}] \approx f(n''_{opt}) \left[\sum_{i=1}^{N_{\boldsymbol{\theta}}^s} w_i p(\boldsymbol{\theta}^{(i)}) \left[\underbrace{\log p(y^{(i)}|\boldsymbol{\theta}^{(i)})}_{\text{Log-Likelihood}} - \underbrace{\log \left(\sum_{k=1}^{N_{\boldsymbol{\theta}}^s} w_k p(\boldsymbol{\theta}^{(k)}) p(y^{(i)}|\boldsymbol{\theta}^{(k)}) \right)}_{\text{Log-Evidence}} \right] \right] - \mathrm{RCI}. \tag{B1}$$

Considering Equation (B1), the information gain can be viewed as a trade-off between data fitting (likelihood) and evidence. Moreover, if we consider that the measurement error is very low (as for the results shown in Figure 1), we can assume that the data fitting term will be almost the same for every sensor location. As a result, the information gain will be dictated by the value of the evidence for each candidate sensor location, which is in turn related with the ToF ellipses. Let us illustrate this trade-off in practice using the following examples:

Example 1. If we consider a sensor located at (0.25 m, 0.06 m) and an actuator at (0.35 m, 0.16 m), we can build the ellipses from the ToF model that passes through the four damage samples, as shown in Figure B1a. Note that in this case, there are two ellipses overlapping. When this happens, two of the addends in the evidence summation (Equation B1) have nonzero likelihood values $p(y^{(i)}|\boldsymbol{\theta}^{(k)})$, which correspond to the damage samples $\boldsymbol{\theta}$ that have been crossed by the same ellipse. This fact makes the evidence term to be relatively high when compared to any other sensor location and therefore makes the information gain lower.

Example 2. Considering the same locations for the actuator and damage samples as in the previous example, but with a different sensor location (0.33 m, 0.20 m), the new nonoverlapping ellipses are shown in Figure B1b. In this case, only one of the addends in the evidence summation (recall Equation B1) is nonzero, which makes the evidence term smaller. Given that the likelihood or data fitting remains almost the same as in Example 1 (due to the very small measurement error) and that the evidence is lower in this case, this candidate sensor location have a higher information gain.

B.2 | Intermediate value of the measurement error

When the measurement error has an intermediate value, the optimal sensor location is given by a single point, which is different from the optimal location from very low or very high values of the measurement error. To better understand the reasons why this occurs, we consider the optimal sensor placement shown in Figure 2a for $\overline{\sigma} = 1\text{e-}6\,\text{s}$, which is located at the coordinates (0.27 m, 0.20 m). Additionally, we consider another suboptimal sensor location for the same measurement error scenario for comparison purposes, for example, (0.335 m, 0.20 m).

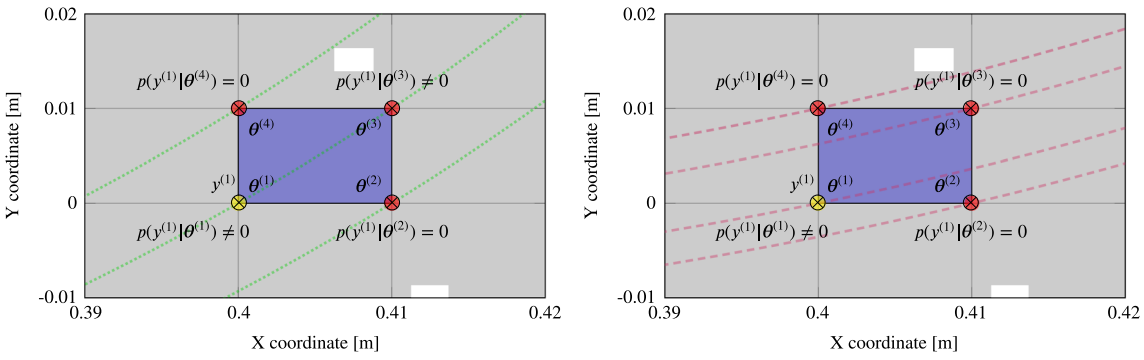

(a) Ellipses for sensor placed at (0.25m, 0.06m)

(b) Ellipses for sensor placed at (0.33m, 0.20m)

FIGURE B1 Decomposition of the evidence summation term of Equation (B1) for two candidate sensor locations. (a) For a low-informative sensor location and (b) for an high-informative sensor location

In this context, and based on the previous subsection, the new ellipses are shown in Figure B2. It can be observed that the optimal sensor location provides elliptic bands that are almost equidistant (Figure B2a). Note that in this scenario, the elliptic curves are transformed into elliptic bands given that the measurement error, hence, the uncertainty, has increased. These elliptic bands depict the increased width of the likelihood function. Therefore, when the evidence term is evaluated (recall Equation B1), that is, by considering one ellipse ($y^{(i)}$) and evaluating all the samples ($\boldsymbol{\theta}^{(k)}$), the result is smaller for the case where these elliptic bands are farther between them (see Figure B2a). Besides, as the likelihood term of Equation (B1) is relatively similar for different sensor locations, the information gain is higher when the elliptic bands are the farthest between each other. Any other suboptimal sensor location provides a higher term of the evidence given that the elliptic bands are closer, if not overlapping, as shown in Figure B2b. This, in turn, produces a higher evidence and lower information gain.

B.3 | High value of the measurement error

Finally, when the measurement error is relatively high, the elliptic bands shown above end up overlapping for all candidate sensor locations as depicted in Figure B3. In these cases, the evidence is higher for the sensor located at (0.27 m, 0.20 m) (Figure B3a), as the contribution for each damage sample ($\boldsymbol{\theta}^{(k)}$) when evaluating one ellipse ($y^{(i)}$) is higher, and consequently, the information gain is smaller.

Conversely, the previous suboptimal sensor location for an intermediate value of the measurement error, that is, (0.335 m, 0.20 m), provides here the most informative scenario, hence being the optimal location for higher values of measurement error (i.e., $\overline{\sigma} \geq$ 1e-5 s as shown in Figure 2a). As depicted in Figure B3b, this candidate sensor location also provides elliptic bands that are overlapping; however, there is a higher difference between two of them, which causes them to have a smaller evidence and hence the highest information gain.

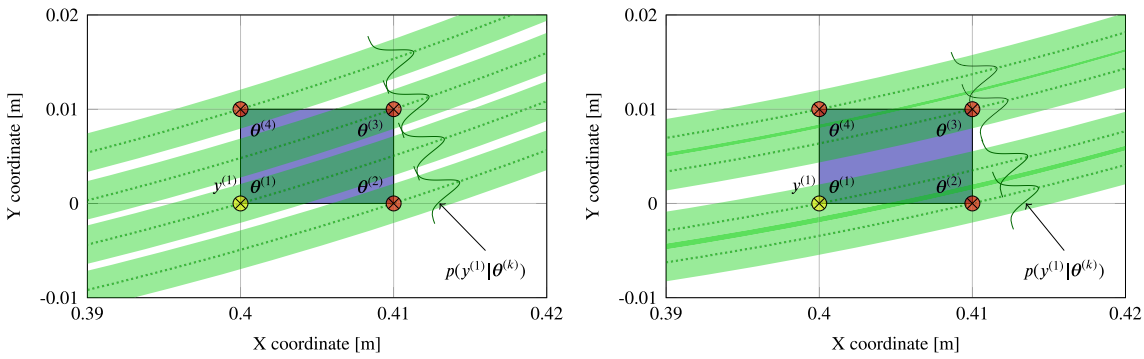

(a) Ellipses for sensor placed at (0.27m, 0.20m)

(b) Ellipses for sensor placed at (0.335m, 0.20m)

FIGURE B2 Schematic representation of elliptic bands for an intermediate value of the measurement error

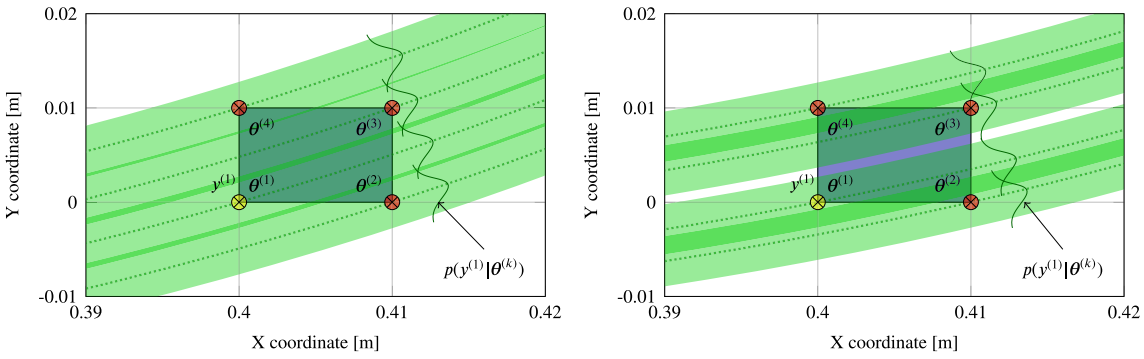

(a) Ellipses for sensor placed at (0.27m, 0.20m)

(b) Ellipses for sensor placed at (0.335m, 0.20m)

FIGURE B3 Schematic representation of elliptic bands for a high value of the measurement error